Spring 2017

Pushing the limits of spectroscopic imaging using novel low-rank based reconstruction algorithm

Ipshita Bhattacharya
University of Iowa

PUSHING THE LIMITS OF SPECTROSCOPIC IMAGING USING NOVEL LOW-RANK BASED RECONSTRUCTION ALGORITHM

by

Ipshita Bhattacharya

A thesis submitted in partial fulfillment of the
requirements for the Doctor of Philosophy degree
in Electrical and Computer Engineering
in the Graduate College of
The University of Iowa

May 2018

Thesis Supervisor: Professor Mathews Jacob

Graduate College
The University of Iowa
Iowa City, Iowa

CERTIFICATE OF APPROVAL

PH.D. THESIS

This is to certify that the Ph.D. thesis of

Ipshita Bhattacharya

has been approved by the Examining Committee for the thesis requirement for the Doctor of Philosophy degree in Electrical and Computer Engineering at the May 2018 graduation.

Thesis Committee: _____
Mathews Jacob, Thesis Supervisor

_____
Vincent A Magnotta

_____
Daniel Thedens

_____
Christopher M. Cheatum

_____
Raghuraman Mudumbai

ACKNOWLEDGEMENTS

This section would be one of the most important chapters of this thesis. The entire journey of my PhD has been very eventful and a truly humbling experience. Today when I look back I know none of this would have been possible without the help of several people in my life. First I would like to immensely thank my advisor Dr. Mathews Jacob for his help throughout the journey. His countless hours of advising and patience has been a key ingredient in making this thesis possible. From the day I joined his lab he has been supportive when he should have been and given the right push when things were slowing down. I owe it to him for completing this thesis. Thank you Dr. Jacob for believing in me and introducing me to the wonderful world of research.

I would also like to thank my collaborators Dr. Christopher M. Cheatum and Jonathan Humston for helping me understand enough about 2D IR spectroscopy and carrying a very successful collaboration. Many hours of brainstorming with Jon and Dr. Cheatum during the paper reviews and the trips to IATL are very important memories of my PhD.

To my committee members, Drs. Vincent Magnotta, Daniel Thedens, Christopher Cheatum and Raghuraman Mudumbai, thank you for taking pains to understand my research and offer valuable insights and corrections to improve the quality of this work.

I am also very appreciative of Marla Kleingartner, Autumn Craig, and Kori Rich, the MR research technologists at the University of Iowa Magnetic Resonance Research Facility for their patient help with the scans.

My stay in Iowa City and going through all the ups and downs would not have been possible without the help of some people. They have supported me in all other ways possible. Firstly Cathy Kern, our department secretary was always my go-to person no matter what the situation. Dina for helping out numerous times with the

administrative procedures.

Past and present CBIG lab members for pumping each other up during deadlines and such wonderful memories. I can say for sure we have one of the most dynamic and supportive set of lab members and that is a lot for making the journey enjoyable.

My life in Iowa City would have been impossible without the support of my friends here, who are like family to me. Phatak, Kashyap, Vishwa, Nirmal, Oishik, Sampada, Apoorva, Sujit, Nidhi you all have played a very active part in keeping me sane and motivated during this journey. I might be mentioning just their names here but their contribution is beyond words. Thank you for gifting me all the amazing memories for a lifetime.

Finally the people who gave me courage from 8500 miles away. My parents who always supported me in every decision and kept me going when I was about to give up. I strive to be worthy of their love and affection but it is hard. Ma and Baba your love and blessings are highly appreciated and this is dedicated to you. My brother who has motivated me to aim high and think high, I thank you for instilling all those values in me since I was a kid. My sister-in-law who has been there throughout, always inspiring me. Also all my relatives and family members and friends who have played a part in shaping me , all of you are somehow responsible for making this happen and I cannot thank you all enough. And finally Almighty or the supreme power, I would like to thank you for teaching me to believe in myself and my efforts when things got rough. This has been a life changing experience.

ABSTRACT

Magnetic Resonance Imaging has been one of the most popular imaging modality providing high resolution anatomical scans. However along with anatomical information the tissue metabolism reveals more intricate information which only manifests as structural changes much later. Magnetic Resonance Spectroscopic Imaging (MRSI) is one such unique technique which simultaneously achieves structural and bio-chemical information. However the clinical appeal is restricted due to many of the limitations particular to spectroscopic imaging.

In this thesis such technical challenges were targeted and optimization techniques were developed exploiting data driven models as priors to improve reconstruction and data acquisition of spectroscopic data. Specifically, three problems were looked at which have been particularly challenging for MRSI. In this work methods were developed to increase the spatial resolution and decrease truncation artifacts from high intensity lipids surrounding the brain introducing algorithms for lipid un-suppressed recovery. Secondly structured low-rank algorithm for removal of spurious peaks artifacts in high resolution echo-planar spectroscopic(EPSI) data were developed. Finally novel methods to accelerate multi-dimensional spectroscopy were introduced.

In the first part a novel algorithm is introduced to push the spatial resolution of MRSI data with minimal lipid leakage artifacts, from dual density spiral acquisition. The reconstruction of MRSI data from dual-density spiral data is formulated as compartmental low-rank recovery problem. The MRSI dataset is modeled as the sum of metabolite and lipid signals, each of which are support limited to the brain and extra cranial regions respectively, in addition to being orthogonal to each other. The reconstruction problem is formulated as an optimization problem, which is solved using iterative re-weighted nuclear norm minimization. The comparisons of the scheme against dual-resolution reconstruction algorithm on numerical phantom and *in-vivo* datasets demonstrate the ability of the scheme to provide higher spatial resolution

and lower lipid leakage artifacts. The experiments demonstrate the ability of the scheme to recover the metabolite maps, even from short echo-time lipid unsuppressed datasets. The proposed reconstruction method and data acquisition strategy provides an efficient way to achieve high resolution metabolite maps without lipid suppression. This algorithm is beneficial for fast metabolic mapping and extension to multislice acquisitions.

The second part studies echo-planar spectroscopic imaging (EPSI) sequence which is often spectrally interleaved to rapidly collect metabolic MRI data. The main problem in using it on high field scanners is the presence of spurious peaks resulting from phase distortions between interleaves as well as the low signal to noise ratio. We introduce a novel structured low-rank framework for the simultaneous denoising and deinterleaving of spectrally interleaved EPSI data. The proposed algorithm exploits annihilation relations resulting from the linear predictability of exponential signals as well as due to uncorrected phase relations between interleaves. The algorithm is formulated as a structured nuclear norm minimization of a block Hankel matrix, derived from the interleaves. Experiments using hyperpolarized ^{13}C mouse kidney EPSI data and ^{1}H *in-vivo* EPSI data demonstrate the ability of the algorithm to remove ghost peaks from EPSI data collected using bipolar readout gradients and flyback trajectories.

Finally a computationally efficient structured low rank algorithm for the reconstruction of two-dimensional infrared (2D IR) spectroscopic data from few measurements is introduced. The signal is modeled as a combination of exponential lineshapes, which are annihilated by appropriately chosen filters. The annihilation relations result in a low-rank constraint on a Toeplitz matrix constructed from signal samples, which is exploited to recover the unknown signal samples. Quantitative and qualitative studies on simulated and experimental data demonstrate that the algorithm outperforms the discrete compressed sensing algorithm, both in uniform and non-uniform

sampling settings. The method is also extended to accelerate multidimensional MR spectroscopic data.

PUBLIC ABSTRACT

Non-invasively resolving spatial distribution of tissue metabolites serves as a diagnostic tool to *in-vivo* metabolism thus making magnetic resonance spectroscopic imaging (MRSI) a very useful application. The tissue concentrations of various metabolites reveal disease state and pseudo-progression of tumors. Also, bio-chemical changes manifest much earlier than structural changes that are achieved using standard magnetic resonance imaging (MRI). However, MRSI has not achieved its potential due to several technical challenges that are specific to it. Several technical advances in the field of MRI does not translate to MRSI. The specific limitations which make MRSI challenging include long scan times, poor spatial resolution, extremely low signal to noise ratio (SNR), truncation artifacts, to name a few.

In the last few decades, research in MRSI has focused on advanced data acquisition and reconstruction methods, however they cannot achieve high resolution and feasible scan time. Moreover there are several artifacts that thwart the increase of spatial resolution not to mention extremely low SNR. Existing methods cannot deal with these limitations which considerably impacts applications of MRSI. In this thesis work these problems are revisited and data acquisition and reconstruction techniques are introduced to address several such challenges.

In the first part of the thesis a variable density spiral acquisition technique is developed which achieves high SNR corresponding to metabolites of interest while reducing truncation artifacts. Along with that we develop a novel compartmentalized reconstruction framework to recover high resolution maps from lipid unsuppressed data. Avoiding lipid suppression not only reduces scan time and reliability but also improves SNR which is otherwise reduced even further with existing lipid suppression methods. The proposed algorithm exploits the idea that the lipid and metabolite compartment reside in low-dimensional subspace and orthogonality priors are used to reduce overlap of subspaces.

This work also explores spectral artifacts like Nyquist ghosting which is a common problem with spectral interleaving. Especially in echo-planar spectroscopic imaging (EPSI), one of the most popular MRSI techniques, maintaining a spatial and spectral resolution requires interleaving. Due to scanner inconsistencies spurious peaks arise which makes quantification inefficient. In this thesis a novel structural low-rank prior is used to reduce and denoise spectra and achieve high resolution ESPI data.

Finally part of this thesis is dedicated to accelerating multi-dimensional spectroscopic problems. Resolving spectra in two dimensions can help study overlapping spectra and achieve more insight. However with an increased dimension the scan time increases. An algorithm for accelerating this method is developed by recovering data from undersampled measurements.The performance of the algorithm is demonstrated for two applications, 2D infra red spectroscopy and 2D MR spectroscopy .

The aim of the thesis is to solve these challenges in MRSI from a signal processing perspective and be able to achieve higher resolution data in practical scan time to ultimately help MRSI reach its potential.

TABLE OF CONTENTS

LIST OF FIGURES

Figure

CHAPTER 1
INTRODUCTION

Magnetic resonance imaging (MRI) has been a versatile clinical tool since its inception and has revolutionized medicine by providing a non-invasive method diagnostic and prognostic assessment *in-vivo* without the bane of exposure to harmful radiation. Even though traditional MRI is unparalleled in its ability to provide complementary tissue contrasts highlighting specific anatomical features or impairment, another dimension of information lies in the tissue metabolite content which can be probed using magnetic resonance spectroscopic imaging (MRSI). MRSI consolidates the basic principles underlying MRI, and the spectrally discrimination abilities of nuclear magnetic resonance (NMR) spectroscopy resulting in spatially localized distributions of metabolic content.

MRSI has been identified for its potential to provide complementary information in the study of diseases such as cancer and treatment of brain tumors [47, 84]. For instance contrast-enhanced structural MRI, even though a powerful diagnostic aid, is unable to identify regions of active tumor [48, 87, 90]. However, MRSI has been acknowledged for its discriminating potential of different diagnostics and is proving to be a useful tool for revealing tumor heterogeneity [77,97,104]. Moreover, some studies reveal that extent of high grade gliomas reported by metabolite maps derived from MRSI measurements exceed the pathological volume determined by accompanying structural MR images [93, 105] and are also observed to have correlation with tumor recurrence following radiosurgery [18,39]. The advantage of MRSI is not only limited to brain but has been demonstrated in study of breast [55] and prostate cancer [62, 102], psychiatric conditions [23, 35], neurodegenerative disorders [1, 103], and in the localization of epileptogenic networks and foci [4, 67].

In spite of the promise it offers MRSI has not achieved as much clinical appeal. This is because of several technical limitations which have make it cumbersome to em-

ploy MRSI exams in a practical setting. The following are the fundamental technical limitations.

- **Low signal to noise ratio (SNR):** The metabolites of interest to be imaged in MRSI are extrememly low in concentration compared to water molecules that are imaged in standard MRI [24]. They are about thousand times smaller in concentration compared to water (see Fig. 1.1(a)). This makes MRSI an imaging modality with extremely low sensitivity.

- **Long data acquisition time:** To counter the SNR limitation, several averages are collected in MRSI studies thus leading to long scan times. Moreover, data needs to be encoded in multiple dimensions, three spatial for full brain and two spectral for multidimensional MRSI, making it extremely slow. This significantly prolongs the data acquisition limiting the practical utility.

- **Poor Spatial Resolution:** To reduce scan time MRSI methods are restricted to limited number of spatial encodes and obtain reconstruction with large voxel size so as to get enough signal. This results in severe voxel interference restricting proper spatial resolution of spectroscopic information. As shown in Fig. 1.1(b) metabolite maps have very low resolution compared to standard MRI on the left.

- **High intensity nuisance signals :** MRSI experiments face the challenge of dealing with high intensity nuisance signals like water and lipids which overpower the signals of interest. These signals if not removed can have detrimental effects on the estimation of metabolic information. Fig. 1.2 exhibits some common lipid suppression methods.

- **Long experimental time for multi-dimensional spectroscopy:** Linear or 1-dimensional spectroscopy is often incapable of distinguishing ambiguous spectral features. These embarrassing ambiguities of one-dimensional spectroscopy

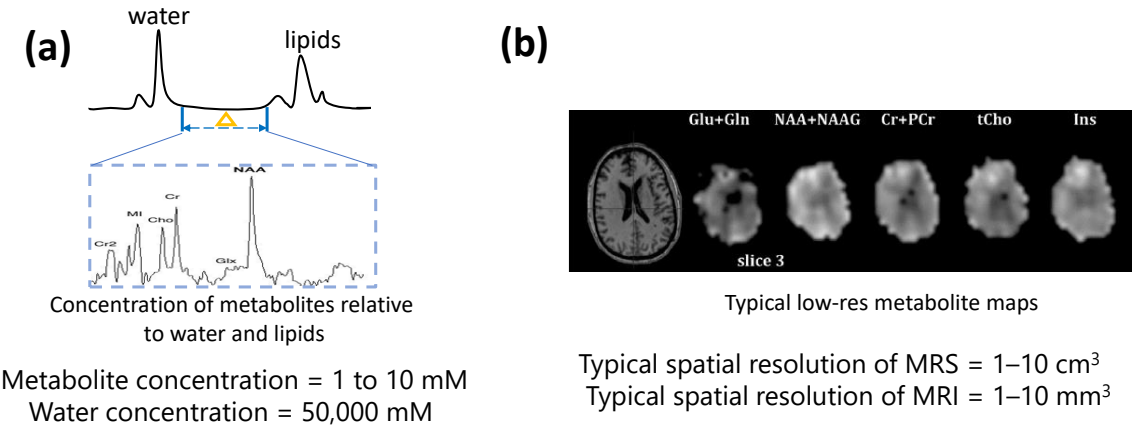

Figure 1.1: Low SNR and resolution of metabolites: (a) Metabolites of interest are SNR starved in comparison to water and lipid signals in the brain. It is about 5000 times smaller in concentration. (b) Typically voxel sizes for MRSI are much larger compared to MRI to boost SNR. This results in low resolution images. No spatial details can be observed in the metabolite maps whereas the MRI scan on the left has high resolution details.

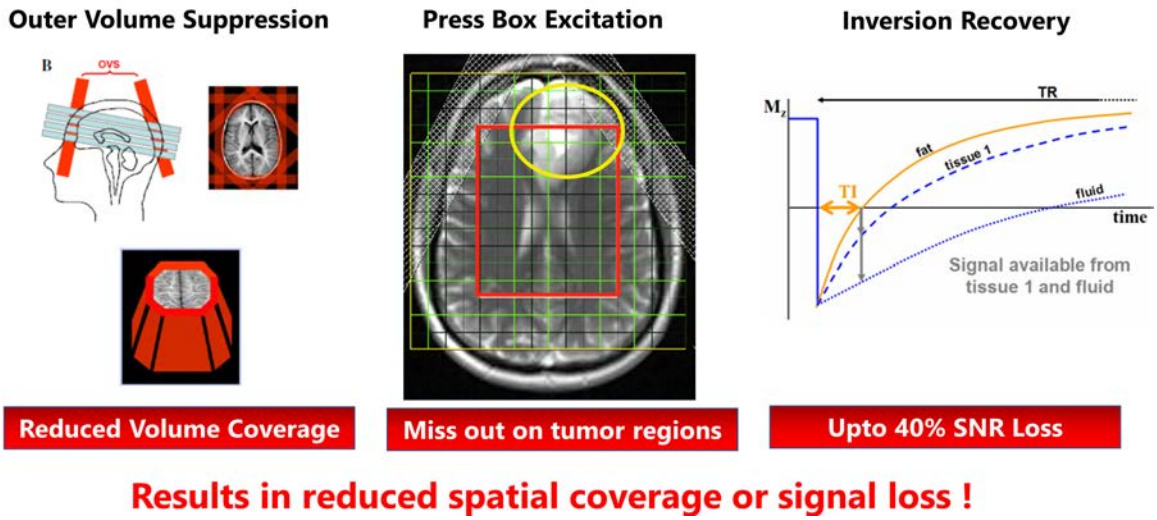

Figure 1.2: Lipid suppression methods: Several methods have been developed to remove nuisance lipid signals during the data collection step. Unfortunately they come with limitations like reduced volume coverage and further reduction of SNR.

can be overcome using multidimensional spectroscopy (MuDSy) where cross-peaks in the 2D spectrum directly map to couplings that are highly dependent on distance and angular orientation. However increased dimensions increases scan time.

These consideration and several other practical constraints related to expected patient compliance, thus command considerable compromises in terms of comprehensiveness of the measurement process and the overall scan time. Therefore, translation of MR spectroscopic exams to regular clinical practice is challenging and less prevalent.

Over the last few decades several attempts have been made to improve MRSI. Efforts have been made to improve hardware such as high field scanners and parallel transmit/receive arrays. Many fast scanning procedures and data acquisition methods have been developed, even though these methods reduce scan time it comes at the expense of SNR. A number of advanced reconstruction methods have been developed exploiting prior information to compensate for lack of SNR. They exploit anatomical priors, sparsity and low-rank constraints and parametric models to recover from noisy and undersampled measurements. However reconstruction methods have not addressed some of the concerns which need to be solved for MRSI to gain momentum.

1.1 Contribution

In this thesis we develop several optimization and reconstruction techniques to answer several technical concerns.

- **Compartmentalized model for lipid unsuppressed reconstruction:** We combine the dual-density spiral MRSI acquisition method with a novel compartmentalized low-rank algorithm to recover metabolic images with higher spatial resolution and minimal lipid leakage artifacts. We model the field inhomogeneity compensated dataset as the sum of metabolite and lipid signals, each

of which are only non-zero within the brain and extra-cranial regions, respectively. Since each of these signals arise from finite number of anatomical regions with distinct spectral signatures, they can each be efficiently represented as the linear combination of finite number of basis functions. We propose to organize the metabolite and lipid signals as low-rank matrices, and their recovery from noisy measurements can be regularized using nuclear norm penalties.

- **Removal of spurious peaks due to spectral interleaving:** We introduce a novel reconstruction method for EPSI data which does not depend on accurate estimates of phase inconsistencies or k-t space trajectory to suppress the spectral ghosts. We exploit the annihilation relations in spectrally interleaved EPSI data resulting from the linear predictability of exponential signals and phase relations between the interleaves. We pose the problem as a recovery of two signals at each pixel, corresponding to the odd and even interleaves. We rely on the annihilation property due to linear predictability of the exponentials. We construct a block Hankel matrix, whose entries correspond to the two echoes, that capture the annihilation relations in a compact way; the annihilation relations translate to a low-rank block Hankel matrix, which we recover from undersampled measurements using structured nuclear norm minimization.

- **Accelerated reconstruction of multi-dimensional spectroscopy:** We introduce a computationally efficient structured low rank algorithm for the reconstruction of two-dimensional infrared (2D IR) spectroscopic data from few measurements. The signal is modeled as a combination of exponential lineshapes, which are annihilated by appropriately chosen filters. The annihilation relations result in a low-rank constraint on a Toeplitz matrix constructed from signal samples, which is exploited to recover the unknown signal samples. Quantitative and qualitative studies on simulated and experimental data demonstrate

that the algorithm outperforms the discrete compressed sensing algorithm, both in uniform and non-uniform sampling settings.

1.2 Organization of the Thesis

The thesis is organized as follows.

Chapter 2 introduces the compartmentalized low-rank based model developed for reconstruction of high resolution MRSI data and removal of lipid leakage artifacts. We also introduce a novel approach for collecting dual denisty spiral data. Chapter 3 describes a structured low-rank model we developed for removal of spurious Nyquist ghosts arising in the spectral domain due to spectral interleaving. We specifically evaluate the performance for EPSI data acquisition. Chapter 4 describes a method for accelerating multi-dimensional spectroscopy while preserving lineshapes. Optical spectroscopy experiments such as 2D infra-red spectroscopy spectroscopy is a tool we use to study transient molecular structure and dynamics in solution. As a vibrational spectroscopic method, it directly interrogates the vibrations of chemical bonds and how the vibrations interact with one another. The proposed method is able to retrieve lineshapes at high acceleration factors making experiments feasible. Finally 5 concludes the research and highlights future directions for this research.

CHAPTER 2
COMPARTMENTALIZED LOW-RANK RECOVERY FOR HIGH RESOLUTION LIPID UNSUPPRESSED MRSI

2.1 Introduction

MR Spectroscopic Imaging (MRSI) enables the spatial mapping of multiple tissue metabolites *in vivo*, many of which are proven to be valuable biomarkers for several diseases [36, 37, 80]. However, the clinical utility of MRSI is currently restricted by several challenges, resulting from very low metabolite concentrations. Specifically, the achievable spatial resolution using Nyquist sampling and conventional recovery schemes is limited by SNR of the metabolites and scan time. The broad point spread functions result in significant spectral leakage from the extra cranial lipid signals and residual water signals, which have several orders of magnitude higher intensity than metabolites.

Several water and lipid suppression schemes are available in MRSI. The chemical-shift selective saturation methods [25, 41, 86], followed by post processing methods such as Hankel singular value decomposition (HSVD) [7] can provide reasonable suppression of the residual water signal. Popular approaches to attenuate lipid signals include outer volume suppression (OVS) [21, 28, 65, 74], inversion recovery [16, 29, 61], inner volume excitation [14, 15], and the use of long echo times [75, 100]. None of these methods provide perfect suppression of lipids, in addition results in signal loss or reduced brain coverage. Moreover, many of these methods have limitations in the practical setting. For example, the placement of the OVS bands may be challenging and time consuming for multislice acquisitions and also be limited by allowable RF energy deposition limits at higher field strengths. The performance of many of the above methods (e.g. OVS, inner volume excitation) are also degraded in the presence of field inhomogeneity and chemical shift effects, especially at high field strengths.

Since the above methods do not perfectly suppress lipids, post-processing methods were introduced to further minimize the residual lipids. A popular approach is to

use k-space extrapolation using the high-resolution spatial support estimates [46,94]. This method provides acceptable spectral quality, when combined with inversion recovery lipid suppression [79]. Several authors have proposed dual-density acquisition methods, coupled with dual-resolution reconstruction algorithms, to further improve lipid suppression. The basic idea is to extend the k-space coverage to obtain narrower point spread functions, which will translate to reduced lipid leakage [49,50,52,82,100]. However, high resolution is not SNR efficient for weak metabolite signals since they cannot be recovered reliably from small voxels in a short acquisition time. Dual resolution schemes acquire the central k-space regions with more averages, while the outer k-space is sampled using fast trajectories. The data is recovered using dual-resolution reconstruction algorithms which estimate the metabolite regions (within the brain) at a lower resolution, while the lipid regions are estimated at a high spatial resolution. The recovery of the lipid regions at high spatial resolution results in reduced lipid leakage to regions within the brain. Since the lipid signal is considerably stronger than the metabolites, the acquisition of outer k-space with lesser averages is often sufficient to determine it accurately. While similar dual-resolution algorithms have been successfully used by multiple researchers [11,32], all of them need to be coupled with some form of lipid suppression. In addition, most of these methods are associated with smoothness priors, which result in low-resolution recovery of the metabolite regions. To overcome such limitations recent works have focused on super-resolution recovery of MRSI data. An overview of such super-resolution methods in MRSI is available in [56,59].

In this work [9,10], we combine the dual-density spiral MRSI acquisition method with a novel compartmentalized low-rank algorithm to recover metabolic images with higher spatial resolution and minimal lipid leakage artifacts. We model the field inhomogeneity compensated dataset as the sum of metabolite and lipid signals, each of which are only non-zero within the brain and extra-cranial regions,

respectively. Since each of these signals arise from finite number of anatomical regions with distinct spectral signatures, they can each be efficiently represented as the linear combination of finite number of basis functions. We propose to organize the metabolite and lipid signals as low-rank matrices, and their recovery from noisy measurements can be regularized using nuclear norm penalties. Similar low-rank methods have been recently introduced for signal recovery in many areas, including MRSI [57, 58, 63, 64, 75, 85] and dynamic imaging [17, 42, 70, 71, 111]. Since low-rank penalties do not explicitly impose spatial smoothness, the proposed scheme can minimize the blurring of the metabolite signals associated with dual-resolution recovery methods such as [11, 13, 32, 49, 50, 52, 82, 100]. The spectral signatures of the metabolites and lipid signals are drastically different with different chemical shifts and T_2 decay rates, and hence spectral broadening. Inspired by the work of Bilgic *et al.* [13], we propose to decouple the subspaces without using the information of the spectral support of lipids and metabolites. We consider the subspaces to be mutually orthogonal. We designed a variable density spiral sequence using the numerical algorithm in [92]. This sequence enables us to acquire a 128x128 matrix with 288 radio-frequency excitations in 7.2 minutes of acquisition time. The sequence acquires the central k-space regions with 12 fold oversampling, while the outer k-space regions are acquired at Nyquist sampling rate. The spiral sequence is a better alternative to Cartesian dual-density acquisitions that combine data from separate scans [30, 63, 75, 82]; since all the data is acquired using a single sequence, no correction methods are needed.

We compare the performance of the proposed scheme to our dual-resolution reconstruction scheme that relies on compartmental smoothness priors [32]. A simulated phantom and *in-vivo* data with and without lipid suppression and TE=55 ms was used to validate the method. The experiments show that the proposed method can provide improved reconstruction than dual-resolution recovery schemes. Specifically, it yields metabolite maps with higher resolution and minimal lipid artifacts, even

when no lipid suppression is used.

2.2 Theory

We denote the underlying spatio-spectral function in MRSI by $x(\mathbf{r}, f)$, where $\mathbf{r}$ is the spatial index and f is the spectral index. The measured signal from the j^{th} coil in $k-t$ space is modeled as,

$$\hat{s}_j(\mathbf{k}, t) = \int_{\mathbf{r}\in\Omega} \int_f x(\mathbf{r}, f)\ c_j(\mathbf{r}) e^{-i2\pi\mathbf{k}\mathbf{r}} e^{-i2\pi(f+\Delta f(\mathbf{r}))t} d\mathbf{r} df + \eta_i(\mathbf{k}, t);\ j = 1, ..\#\text{Ncoils}. \tag{2.1}$$

Here, $\mathbf{r}$ specifies the spatial location and t denotes time. $\Delta f(\mathbf{r}) = \gamma \triangle B_0(\mathbf{r})$ is the field-inhomogeneity induced chemical shift at the spatial location $\mathbf{r}$. $c_j(\mathbf{r})$ is the sensitivity of the j^{th} coil, and $\eta_i(\mathbf{k}, t)$ is the white Gaussian measurement noise. Note that the spatial integral is restricted to Ω, which is a mask that specifies the support of the signal (e.g., head). The entire acquisition scheme can be compactly represented as

$$\mathbf{S} = \mathcal{A}_\Omega(\mathbf{X}) + \boldsymbol{\eta}. \tag{2.2}$$

The operator $\mathcal{A}_\Omega$ includes coil sensitivity encoding, k-space encoding, and spatially varying chemical shift resulting from the field inhomogeneity. $\mathbf{S}$ is a matrix, whose entries correspond to the measured $k-t$ space samples. Here, $\mathbf{X}$ is the $R \times N$ Casorati matrix derived from $x(\mathbf{r}, f)$, whose rows correspond to the N point spectra from pixels within Ω:

$$\mathbf{X} = \begin{bmatrix} x(\mathbf{r}_1, f_1) & x(\mathbf{r}_1, f_2) & \cdots & x(\mathbf{r}_1, f_N) \\ x(\mathbf{r}_2, f_1) & x(\mathbf{r}_2, t_2) & \cdots & x(\mathbf{r}_2, f_N) \\ \vdots & \vdots & \ddots & \vdots \\ x(\mathbf{r}_R, f_1) & x(\mathbf{r}_R, t_2) & \cdots & x(\mathbf{r}_R, f_N) \end{bmatrix} \tag{2.3}$$

Here, R is the number of pixels in Ω. Any ordering of the rows of $\mathbf{X}$ may be considered.

Compartmental low rank MRSI signal model: Several authors have proposed to model the signal $x(\mathbf{r}, f)$ using low-rank methods [58, 85]. Specifically, they assume $\mathbf{X}$ in (2.3) to be low-rank. A challenge with the above modeling is the huge dynamic range of the signals $x(\mathbf{r}, f)$. The extracranial lipid signals are several orders of magnitude stronger than the metabolites; low-rank modeling may result in the lower principal components being captured by the lipid signals to account for the subtle variations in the lipid signal. A high rank representation will hence be needed to accurately represent the metabolites, which may make the model inefficient.

The lipid and metabolite signals that originate from disjoint spatial supports, each have finite number of resonant frequencies arising from finite anatomical regions inside the spatial compartments. We assume that the brain and lipid regions, denoted by Ω_M and Ω_L respectively, to be known *a-priori* from water reference scans. We denote the metabolite and lipid components of $x(\mathbf{r}, f)$ as

$$x_M(\mathbf{r}, f) = x(\mathbf{r}, f) \cdot \chi_{\Omega_M}(\mathbf{r}) \tag{2.4}$$

$$x_L(\mathbf{r}, f) = x(\mathbf{r}, f) \cdot \chi_{\Omega_L}(\mathbf{r}) \tag{2.5}$$

Here, χ_Ω is the characteristic function of the region Ω:

$$\chi_\Omega(\mathbf{r}) = \begin{cases} 1 & \text{if} \quad \mathbf{r} \in \Omega \\ 0 & \text{else.} \end{cases} \tag{2.6}$$

Since the regions Ω_M and Ω_L are mutually exclusive, we have

$$x(\mathbf{r}, f) = x_M(\mathbf{r}, f) + x_L(\mathbf{r}, f). \tag{2.7}$$

Note that the dynamic range of the signals x_M and x_L are individually small, even though the dynamic range of the signal x is very high. We construct matrices $\mathbf{X}_M$

and $\mathbf{X}_L$ similar to (2.3) from x_M and x_L by including only pixels from Ω_M and Ω_L, respectively. We assume that $\mathbf{X}_M$ and $\mathbf{X}_L$ are individually low-rank; the compartmental low-rank model allows these matrices to be represented using distinct basis functions and to independently control their ranks.

We observe that the spectra of the metabolite and lipid regions are highly dissimilar, and hence orthogonal (i.e., $\langle x_L(\mathbf{r}_1, f), x_M(\mathbf{r}_2, f)\rangle = 0;\ \forall \mathbf{r}_1, \mathbf{r}_2$). We are inspired by the use of a similar prior in [13] to minimize the cross-talk between x_M and x_L. Combining this prior with the decomposition in (2.7), we obtain

$$\mathbf{X} = \mathbf{X}_M + \mathbf{X}_L; \quad \mathbf{X}_L\, \mathbf{X}_M^H = \mathbf{0}, \tag{2.8}$$

where $\mathbf{X}^H$ is the conjugate transpose of the matrix $\mathbf{X}$.

Recovery of the compartmental signal model from k-t space data: We pose the recovery of the metabolite and lipid components from measured k-space data as the optimization problem:

$$\{\mathbf{X}_M, \mathbf{X}_L\} \;=\; \arg\min_{\mathbf{X}_L, \mathbf{X}_M} \underbrace{\|\mathcal{A}_{\Omega_M}(\mathbf{X}_M) + \mathcal{A}_{\Omega_L}(\mathbf{X}_L)) - \mathbf{S}\|^2}_{\text{data consistency}} \;+\; \underbrace{\lambda_1\|\mathbf{X}_M\|_* \;+\; \lambda_2\|\mathbf{X}_L\|_*}_{\text{low-rank priors}}, \quad \text{such that} \quad \underbrace{\mathbf{X}_M \perp \mathbf{X}_L}_{\text{orth. constraint}}. \tag{2.9}$$

Here $\|\mathbf{X}\|_*$ denotes the nuclear norm of $\mathbf{X}$. The first term is the data consistency term, while the second and third terms are the low-rank priors on the metabolite and lipid signals, respectively. Note that we do not explicitly use the spectral priors of the metabolite and lipid regions to discourage the cross-talk as in [63, 75]; the cross-talk is automatically minimized by the use of the orthogonality priors. As shown in [13], the use of the orthogonality priors will only cause minimal biases in the metabolite signals. Note that we do not use detailed anatomical priors such (e.g. masks of gray matter, white matter, and CSF regions) as proposed by several

authors [6, 32, 51, 54, 56, 60, 72, 91]. However the above framework may be modified to include such detailed anatomical information; we do not consider such priors to minimize the risk of introducing biases. We replace the orthogonality constraint in (2.9) by a penalty. Specifically, the inner-product between the metabolite and lipid signals are penalized, weighted by a high regularization parameter β. The penalty term would reduce to a constraint when $\beta \to \infty$.

We propose to solve the above problem using the iterative re-weighted least square minimization (IRLSM) algorithm [34] for nuclear norm minimization. This approach relies on approximating the nuclear norm penalty at the n^{th} iteration as the weighted Frobenius norm:

$$\|\mathbf{X}\|_1 \approx \|\mathbf{X}\ \mathbf{Q}\|_{\mathbf{F}}^2, \tag{2.10}$$

where the weight matrix at the n^{th} iteration is chosen as $\mathbf{Q} = \left(\mathbf{X}_{n-1}^H \mathbf{X}_{n-1}\right)^{-1/4}$; where $\mathbf{X}_{n-1}$ is the solution of the nuclear norm minimization problem at the $(n-1)^{\text{th}}$ iteration. The matrix power is evaluated using eigen value decomposition. Specifically, we perform eigen decomposition to obtain $\left(\mathbf{X}_{n-1}^H \mathbf{X}_{n-1}\right) = \mathbf{U}\mathbf{\Sigma}\mathbf{U}^H$ and complete the weight matrix as $\mathbf{Q} = \mathbf{U}\mathbf{S}\mathbf{U}^H$, where $\mathbf{S} = \mathbf{\Sigma}^{-(1/4)}$. To avoid division by zero, the diagonal entries of $\mathbf{S}$ are stabilized as $s_i = \max\left(\sigma_i, \epsilon\right)^{-(1/4)}$, where ϵ is a stabilization constant. For the convergence of the solution, we require $\epsilon \to 0$ as $n \to \infty$. When a target rank K is desired, the stabilization parameter is chosen as $\epsilon = \gamma\ \sigma_K$, where $0 < \gamma < 1$. See [34, 83] for details of the IRLSM scheme.

Using the IRLSM scheme to solve (2.9) amounts to solving the following quadratic criterion at the n^{th} iteration:

$$\begin{aligned}\{\mathbf{X}_L, \mathbf{X}_M\}_n = \arg\min_{\mathbf{X}_L, \mathbf{X}_M} \|\mathcal{A}_{\Omega_M}(\mathbf{X}_M) + \mathcal{A}_{\Omega_L}(\mathbf{X}_L)) - \mathbf{S}\|^2 \ &+\ \lambda_1 \|\mathbf{X}_M\ \mathbf{Q}_M\|_F^2 \\ &+\ \lambda_2 \|\mathbf{X}_L\ \mathbf{Q}_L\|_F^2 \ +\ \underbrace{\beta \|\mathbf{X}_M\ \mathbf{Q}_O\|_F^2}_{\text{orthogonality penalty}}. \end{aligned} \tag{2.11}$$

The weight matrices matrices $\mathbf{Q}_M$ and $\mathbf{Q}_L$ are updated at the n^{th} iteration using the solutions $\{\mathbf{X}_M, \mathbf{X}_L\}_{n-1}$ as

$$\mathbf{Q}_M = \mathbf{U}_M \, \tilde{\mathbf{\Sigma}}_M^{(-1/4)} \, \mathbf{U}_M^H, \quad \text{where} \quad \mathbf{X}_M \mathbf{X}_M^H = \mathbf{U}_M \mathbf{\Sigma}_M \mathbf{U}_M^H \tag{2.12}$$

$$\mathbf{Q}_L = \mathbf{U}_L \, \tilde{\mathbf{\Sigma}_L}^{(-1/4)} \, \mathbf{U}_L^H, \quad \text{where} \quad \mathbf{X}_L \mathbf{X}_L^H = \mathbf{U}_L \mathbf{\Sigma}_L \mathbf{U}_L^H. \tag{2.13}$$

The diagonal entries of the matrices $\tilde{\mathbf{\Sigma}}_M$ and $\tilde{\mathbf{\Sigma}}_L$ are stabilized versions of the entries of $\mathbf{\Sigma}_M$ and $\mathbf{\Sigma}_L$, respectively, to avoid division by zero; i.e, $\tilde{\mathbf{\Sigma}}(i) = \min(\mathbf{\Sigma}(i), \epsilon)$. Equation (2.11) may be intuitively interpreted. If the matrices $\mathbf{X}_M$ and $\mathbf{X}_L$ are low-rank and the singular values decay rapidly, $\mathbf{Q}_M$ and $\mathbf{Q}_L$ are projection operators onto the noise subspaces of $\mathbf{X}_M$ and $\mathbf{X}_L$ (corresponding to insignificant singular values), respectively. Thus, the second and third terms enable denoising by minimizing the projection of the signals to the null-spaces, estimated from the previous iteration. The projection matrix for orthogonality constraint $\mathbf{Q}_O$ in (2.11) is obtained as

$$\mathbf{Q}_O = \mathbf{U}_L \, \mathbf{\Sigma}_L^{(1/2)} \, \mathbf{U}_L^H, \quad \text{where} \quad \mathbf{X}_L \mathbf{X}_L^H = \mathbf{U}_L \mathbf{\Sigma}_L \mathbf{U}_L^H \tag{2.14}$$

2.3 Methods

2.3.1 Variable Density Spiral Spin-Echo Sequence

The k-space trajectories are designed using the numerical algorithm described in [92]. We assumed a matrix size of 128×128 and designed a variable density spiral trajectory with 24 interleaves such that the lower k-space region of radius less than 16 is sampled at the Nyquist rate, while the higher k-space region is sampled at $\frac{1}{12}$ times Nyquist rate. We used the above multishot trajectory with 12 averages. At each average, we rotate the trajectories by $\frac{2\pi}{24 \times 12}$ degrees. The acquisition scheme thus corresponds to twelve fold averaging of the central k-space regions, while the higher k-space region is Nyquist sampled. The above acquisition scheme can also be thought of as a variable density spiral trajectory with $24 \times 12 = 288$ spatial interleaves. The

large number of spatial interleaves ensures that each interleave, along with the k-space rewinders will be completed in 1.74 ms, which corresponds to a spectral bandwidth of 574.7 Hz (4.7 ppm). We use 256 temporal interleaves to achieve a spectral resolution of 2.2 Hz. The k-space acquisition corresponds to three regions (a) lower k-space region, whose acquisition takes around 35% of sampling time, (b) higher k-space regions, which takes around 24% of time, and (c) gradient ramp down and rewinding, which takes around 41% of time. We assumed a field of view of 240 mm, maximum gradient amplitude of 22.4 mT/m, and a slew rate is 125 T/m/sec.

The sequence is illustrated in Fig. 1.

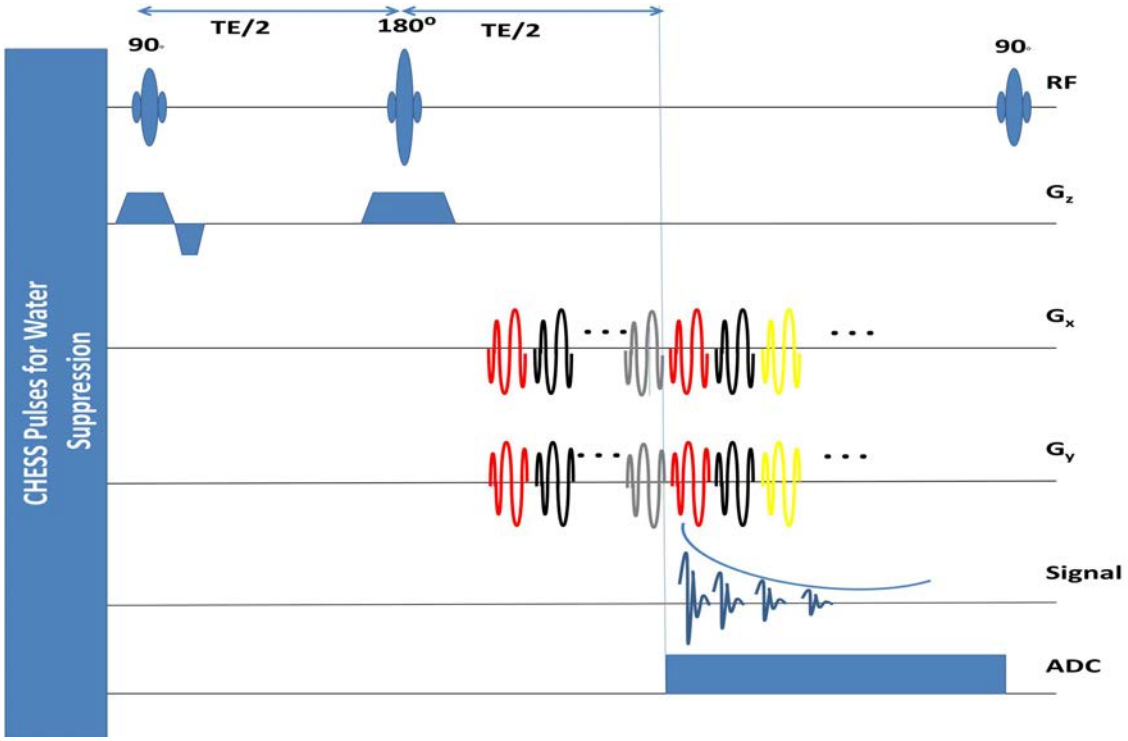

Figure 2.1: Pulse sequence diagram for spin echo based variable density spiral spectroscopic imaging: Water suppression is achieved using CHESS pulses. Slice selective excitation and refocusing RF pulses are applied, followed by repeatedly playing out the spiral gradients, ramp-down gradients, and rewinders.

We use a slice selective spin echo sequence with CHESS water suppression. No lipid suppression is used. The spiral readout and rewinder gradients were repeatedly played out 256 times after an appropriate echo time. TR/TE were chosen to be 1500/55 ms. The total number of RF excitations required were 288 and the total scan time is 7.2 mins. A separate water scan using the same sequence with TR= 500 ms is acquired in 2.4 mins of scan time; the data from this sequence is used to estimate coil sensitivities, field inhomogeneity map, and the spatial supports of lipid and water regions.

2.3.2 Digital Phantom for Validation

We developed a numerical MRSI phantom using the template and code in [40]. This phantom with realistic anatomical features is discretized on a 512×512 Cartesian sampling grid.

We assumed five spatial compartments, as shown in Fig. 3, including two lipid compartments and three brain compartments corresponding to white matter, gray matter and cerebral spinal fluid. We considered three metabolites; NAA at 2.008 ppm, Creatine at 3.027 and 3.913 ppm, and Choline at 3.185 ppm, as described in [38]. Each compartment is assigned metabolite concentrations closely mimicking the expected concentrations in normal brain [107]. A six peak lipid model [110] is used to obtain lipid basis for the lipid compartments. The intensities of the lipid peaks are assigned upto $500 - 1000$ times higher values than metabolites to replicate lipid intensities in brain in absence of any lipid suppression methods and at short TE. We also accounted for the T_2 decay with appropriate parameters, which translates to spectral broadening of the line shapes. We used a B_0 inhomogeneity map using fourth order polynomial in both the spatial dimensions. The Fourier samples of the phantom are numerically evaluated at the k-t space points specified by the above described spiral trajectory. The Fourier samples are corrupted by additive white Gaussian noise.

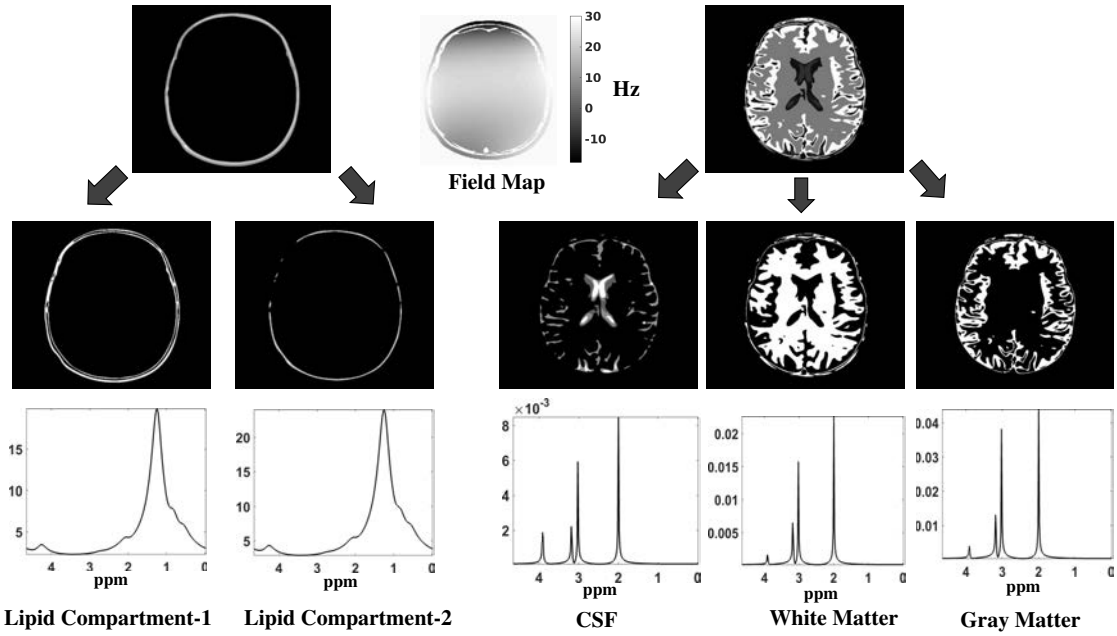

Figure 2.2: Construction of the digital phantom: The phantom is constructed with five different spatial compartmental basis functions (Two lipid compartments, CSF, white matter and gray matter). Each of these compartments have a unique metabolite or lipid spectrum associated with it. The metabolite spectra have peaks corresponding to NAA (at 2.008 ppm), Creatine (at 3.027 and 3.913 ppm) and Choline (3.185 ppm). We choose the concentration of the metabolites in different compartments based on normal brain concentrations reported in literature. The lipid peaks are constructed with a six peak model, reported in [110]. The lipid peaks are chosen to be 500-1000 times larger in amplitude, in accordance to real data without lipid suppression at short TE values. A field inhomogeneity map based on a polynomial model is also used.

To study the effect of lipid suppression, we considered two realizations of the digital phantom **(a)** when the lipid signals are considered to be absent (or lipid compartments are not considered) and **(b)** when the lipid signals are present. The SNR of the k-t space data is 5.26 dB in **(a)** and 26.7 dB in **(b)**; the higher signal energy due to the presence of lipids translates to higher SNR in **(b)**. We compare the performance of Tikhonov regularized method and the proposed low-rank method for both the realizations. The reference reconstruction in the metabolite region is chosen as the gridding reconstruction of the k-t space data, without lipids and additive noise. All the reconstructions are performed on a grid size of 96 $\times$ 96 and a field map is estimated at the same resolution to correct for field inhomogeneity artifacts.

2.3.3 Recovery of MRSI Data Using Other Algorithms for Comparison

We compare the proposed method against the dual-resolution reconstruction scheme, which relies on compartmentalized Tikhonov smoothness regularization [11, 32]:

$$\{\mathbf{X}_M, \mathbf{X}_L\} \;=\; \arg\min_{\mathbf{X}_L,\mathbf{X}_M} \underbrace{\|\mathcal{A}_{\Omega_M}(\mathbf{X}_M) + \mathcal{A}_{\Omega_L}(\mathbf{X}_L) - \mathbf{S}\|^2}_{\text{data consistency}} \;+\; \underbrace{\alpha_1\|\nabla_{\Omega_M}\mathbf{X}_M\|^2 + \alpha_2\|\nabla_{\Omega_M}\mathbf{X}_L\|^2}_{\text{smoothness priors}}.$$

Here, $\nabla_\Omega \mathbf{X}$ denotes the spatial gradient of $\mathbf{X}$, restricted to the spatial compartment Ω. This method penalizes the spatial smoothness of the signal in the two compartments to reduce leakage and cross talk between $\mathbf{X}_L$ and $\mathbf{X}_M$. α_1 and α_2 are spatial regularization parameters that control the resolution/smoothness in the metabolite and lipid compartments, respectively. We consider two different settings for the choice of α_1 for the phantom experiments to demonstrate need for dual-resolution reconstruction and the associated loss in spatial details. We consider a small value of α_1, in this case 10^{-5} , which corresponds to minimal blurring of the metabolites; we refer to this setting as the high resolution (HR) Tikhonov recovery. We also consider a higher value of α_1, in this case 10^{-3}, which provides lower resolution recovery of the metabolites, which is termed as low-resolution (LR) Tikhonov recovery; this is the choice considered

in [32]. These settings translate to point spread function FWHM of 1 pixel and 2.5 pixels, respectively. In both cases, the parameter α_2 is chosen as 10^{-5} to minimize the smoothing of the lipid signals and to minimize the lipid contamination of $\mathbf{X}_M$. We observe that this approach is a variational alternative to iterative methods used in [49, 50, 52, 82, 100].

2.3.4 *In-vivo* Experiments

In-vivo experiments were performed on a 3T Siemens Trio scanner using a 12 channel receive head-coil under a protocol approved by the Institutional Review Board (IRB) of the University of Iowa . Single slice proton MRSI data were collected from two healthy volunteers, after receiving informed consent.

Subject 1: An oblique axial slice above the ventricles was acquired with a FOV of 240×240 mm^2 and a slice thickness of 10 mm . This dataset is used to exhibit the advantage of collecting high resolution encodes in reducing spectral leakage. Water suppression was achieved using CHESS pulses, while the whole slice is excited without any lipid suppression.

Subject 2: An oblique axial slice is selected containing the corpus callosum and the lateral ventricles and was acquired with a FOV of 240×240 mm^2. A lipid suppressed dataset (with eight OVS bands) and another without lipid suppression were acquired.

The high resolution B_0 inhomogeneity map, lipid images and water images are estimated from the water reference data using GOOSE [22]. The water and lipid images are thresholded to derive the lipid region Ω_L and brain regions Ω_M, respectively. These masks are used in (2.9) to define the forward model and to construct the matrices $\mathbf{X}_M$ and $\mathbf{X}_L$. We first performed a gridding recovery, followed by the estimation of the residual water using the HSVD algorithm [7]. The k-space signal corresponding to the residual water signal was subtracted from the measured k-space data before any processing.

We study the benefit in expanding the k-space coverage, using variable density spiral

k-space trajectory in Fig. 2 using data from subject 1.

We truncate the k-space data to different sizes (radius $32, 64, 96$ and 128), which correspond to voxel sizes of $0.56, 0.14, 0.06$ and 0.03 ml, respectively. We recover the data from these four cases using gridding reconstruction algorithm on an image grid size of 128×128. Post recovery, the metabolite data within the brain is smoothed with an iterative algorithm. The smoothing parameters are selected such that the FWHM of the PSF is 2.5 pixels. The NAA images are estimated using peak integration on polynomial baseline suppressed data.

The regularization parameters in the proposed algorithm described in (2.11) are chosen empirically to yield the best results for the experiments on data from subject 2. We observe that the parameter β can be assigned a high value to impose the constraint of lipids being orthogonal to the metabolites; the performance of the algorithm was observed to be relatively insensitive to this parameter, provided it is high enough. As described earlier, λ_1 controls the metabolite denoising, while λ_2 controls the lipid denoising. We observe that high values of λ_2 will result in the attenuation of the lipids in the lipid compartment, which will result in high spectral leakage; the best results are obtained when λ_2 are chosen around 100 fold lower than the value of λ_1. We manually tune the value of λ_1 to get the best compromise between noisy spectra and oversmoothed reconstructions. As described earlier, the choice of the stabilization parameter requires a target rank. We chose the target rank to be 15 for the metabolite signals, and 20 for the lipid signals. The parameter γ in the stabilizing parameter equation $\epsilon = \gamma \sigma_K$, is chosen as 0.8 for both metabolites and lipids. All reconstructions are performed at a grid size of 96×96 and the metabolite maps are obtained by peak integration over a bandwidth of 16 Hz.

2.4 Results

We study the utility of acquiring the data using variable density spiral k-space trajectory with extended k-space coverage in Fig. 2 using data from subject 1. We

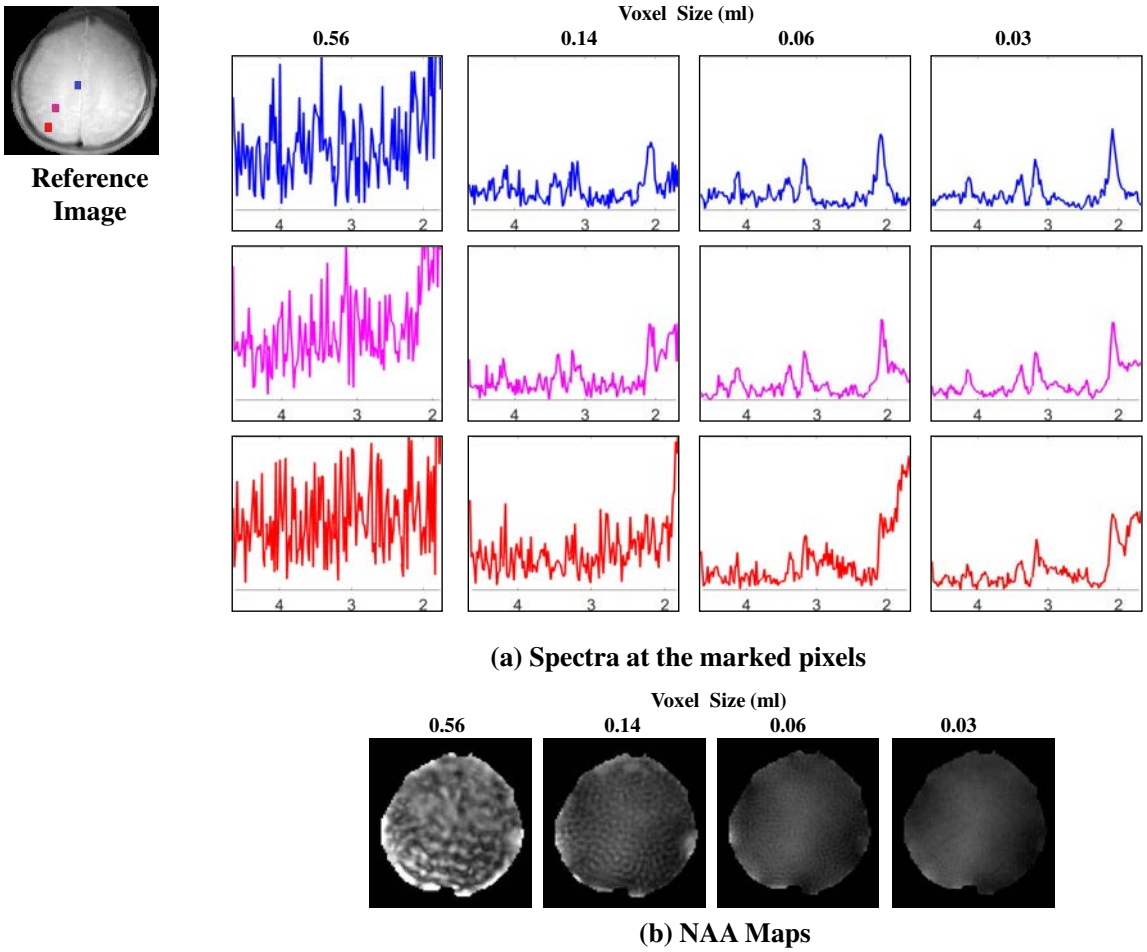

Figure 2.3: Benefit of extended k-space coverage in acquisition without lipid suppression: The top figure (a) shows the spectra at three different locations (blue pixel at the center of the brain, pink pixel between the center and skull, red pixel near the skull or lipid layer). In the absence of lipid suppression, better lineshape and reduction of lipid signal is achieved with increased k-space coverage. The peak integral NAA images in (b) demonstrates the decreased ringing artifacts with increasing k-space coverage.

show the reconstructed spectra from three different pixels within the brain, marked by different colors in the reference image. Since no lipid suppression is used, the spectra with 32x32 spatial coverage is highly distorted at all the three pixels. Specifically, the signals from all the lipid regions with different field inhomogeneity induced shifts leak over to each pixel within the brain; the weighted linear combination of the lipid spectra appear as noise like artifacts. The experiments clearly show the benefit of extended k-space coverage. With higher k-space encodes / smaller voxel size, the spectrum at the blue pixel in the center of the brain are recovered with minimal distortion. The pink pixel closer to the skull exhibits some lipid leakage, while the red pixel close to the skull is corrupted by the extra-cranial lipids even with extended k-space coverage. The reduction in leakage-induced ringing artifacts can also be visualized from the NAA map. Since the extended k-space coverage alone cannot eliminate all the spectral leakage artifacts, we propose to combine it with the compartmentalized low-rank method to further reduce lipid leakage.

The phantom experiment results are shown in Fig. 4. The three methods under comparison are the Tikhonov high resolution (Tikhonov HR) method, Tikhonov low resolution (Tikhonov LR), and the proposed algorithm. The first column corresponds to simulations without any lipid signal (perfect lipid suppression), while the second column is the one with lipid signal (no lipid suppression). For comparisons, we recover a reference data from the signals without any lipids and noise using gridding, followed by field inhomogeneity compensation. The NAA maps for the three methods and their error maps, and spectra at marked pixels are shown in Fig. 4(a) for lipid free simulation and in Fig. 4(b) for simulation with lipids. For the lipid free case, we observe that the Tikhonov HR method results in relatively noisy maps, while the Tikhonov LR method oversmoothes the spatial maps, resulting in systematic loss of edge information, seen from the error maps. The proposed method provides maps with reduced noise and minimal blurring. These results can also be appreciated from

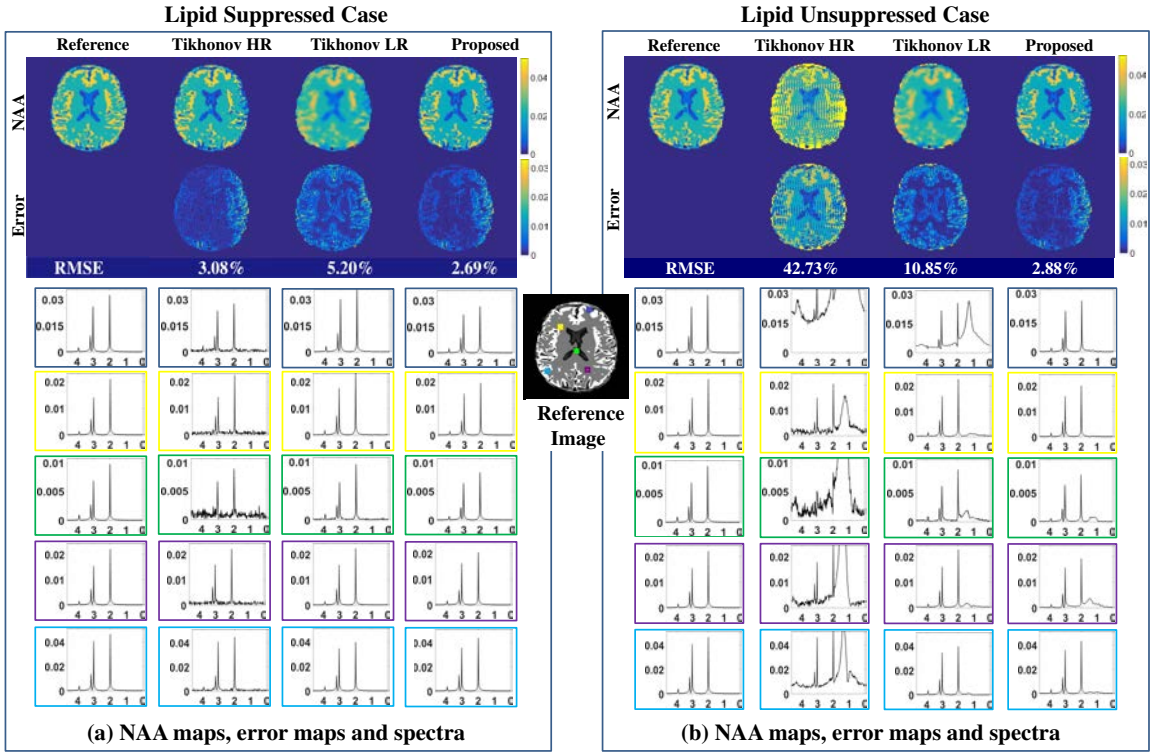

	Lipid Suppressed Case			Lipid Unsuppressed Case		
	Tikhonov HR	Tikhonov LR	Proposed	Tikhonov HR	Tikhonov LR	Proposed
NAA	3.08%	5.20%	2.69%	42.73%	10.85%	2.88%
Creatine	3.29%	6.79%	3.34%	34.06%	10.15%	3.37%
Choline	3.47%	5.54%	2.38%	58.20%	21.54%	2.57%

(c) RMSE table of metabolite maps

Figure 2.4: Simulated phantom experiments: We consider the recovery of the MRSI phantom in Fig. 3 from its noisy k-space measurements on the spiral trajectory. The case without lipid signals (corresponding to perfect lipid suppression) is shown on the left column and the case with lipid signals (no lipid suppression) on the right column. We compare the reconstructions obtained using Tikhonov HR, Tikhonov LR, and the proposed method. The NAA maps and the corresponding error maps (scaled up) for all the methods under comparison with and without lipids are shown in (a) and (b) respectively. Also the spectra at 5 representative locations marked in the reference image are shown for all the methods for lipid free and lipid unsuppressed case in (a) and (b) respectively. The lipid maps for the case without lipid suppression is shown in (d). Table (c) shows the RMSEs for the different maps.

the spectra corresponding to the pixels marked on the reference image. The RMSE (Root Mean Square Error) of the NAA maps are calculated to be 3.08% and 5.20% for Tikhonov HR and Tikhonov LR respectively, while the proposed method has the lowest RMSE of 2.69%. In the lipid unsuppressed phantom experiments shown in the second column, we observe that the Tikhonov HR method is noisy and has severe ringing artifacts (seen from the maps and spectra in Fig. 4(b)). The Tikhonov LR method on the other hand reduces lipid leakage artifacts, but results in blurred maps. It can also be seen from the error maps and the spectra that the pixels closer to the skull have residual lipid artifacts in the Tikhonov LR method. By contrast, the proposed method reduces noise and eliminates artifacts without smoothing the data and retains most of the high resolution details. We observe that the Tikhonov HR method has a poor RMSE of 42.73%, resulting from the extensive lipid leakage. The Tikhonov LR method has a RMSE of 10.85% for NAA maps, while the proposed method maintains a RMSE of 2.88%, which is comparable to the lipid suppressed setting. The RMSEs of other metabolite maps are shown in the Table(c) in Fig. 4. Thus the reconstruction quality of the proposed method is robust even in presence of lipids.The lipid maps obtained by peak integration over lipid resonances are shown in Fig. 4(d) for the lipid unsuppressed case.

The spatial priors and field inhomogeniety map obtained for the *in-vivo* experiments are shown in Fig. 5.

Results for the *in-vivo* experiments with lipid suppression on subject 2 are shown in Fig. 6.

The proposed method is compared against the Tikhonov LR scheme. From Fig. 6(a) it is seen that the Tikhonov regularized method has substantial lipid leakage artifacts. Baseline suppression reduces some lipid leakage, but the maps suffer from spatial blurring. The proposed method on the other hand has negligible lipid leakage artifacts and results in high resolution maps retaining spatial details. Considering that

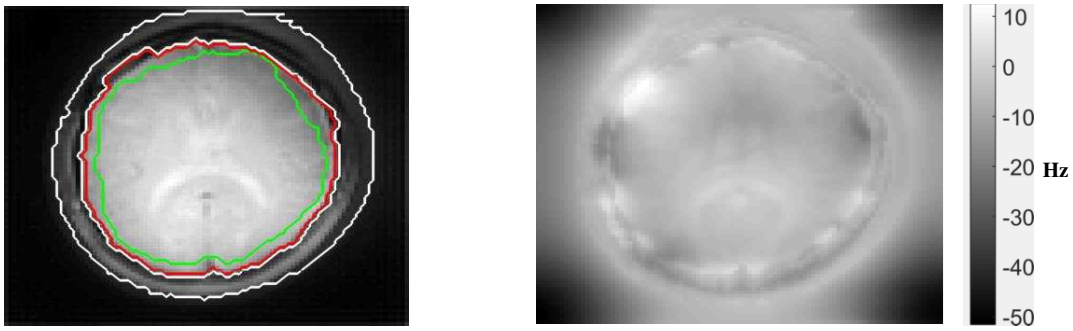

(a) Contours of spatial supports of metabolite and lipids **(b) B_0 inhomogeneity map**

Figure 2.5: Priors estimated from water reference data for subject 2, used by the reconstruction algorithm for the results in Fig. 6 & 7. (a) The contours of the metabolite region without saturation bands is shown in red, while the contour after application of saturation bands is shown in green.The lipid mask contour is outlined in white. The field map recovered from the water reference data is shown in (b).

detailed anatomical priors such as supports of gray matter, white matter, and CSF are not used in the recovery, the ability of the algorithm to recover the spatial details is significant. The lipid maps obtained by peak integration of the lipid resonances are shown for the Tikhonov method and the proposed method. The Tikhonov method shows heavy lipid leakage in regions close to the skull whereas the lipid leakage is negligible for the proposed method. The spectra at the pixel grid marked in the reference image are shown for the Tikhonov regularized method in Fig. 6(b) and for the proposed method in Fig. 6(c). Similar to the results of the phantom simulation, the spectra obtained from Tikhonov method are noisy and have spectral leakage especially in pixels close to the skull. By contrast the proposed method denoises the spectra and removes all spectral leakage. The topmost two pixels close to the skull does not seem to have any metabolite signal, resulting from OVS suppression.

The comparison of the proposed method and the Tikhonov LR method is shown in Fig. 7 for the lipid unsuppressed dataset from the same subject.

The metabolite maps in Fig. 7(a) show quite significant lipid leakage for the Tikhonov regularized method. Even after baseline removal, lipid leakage artifacts are

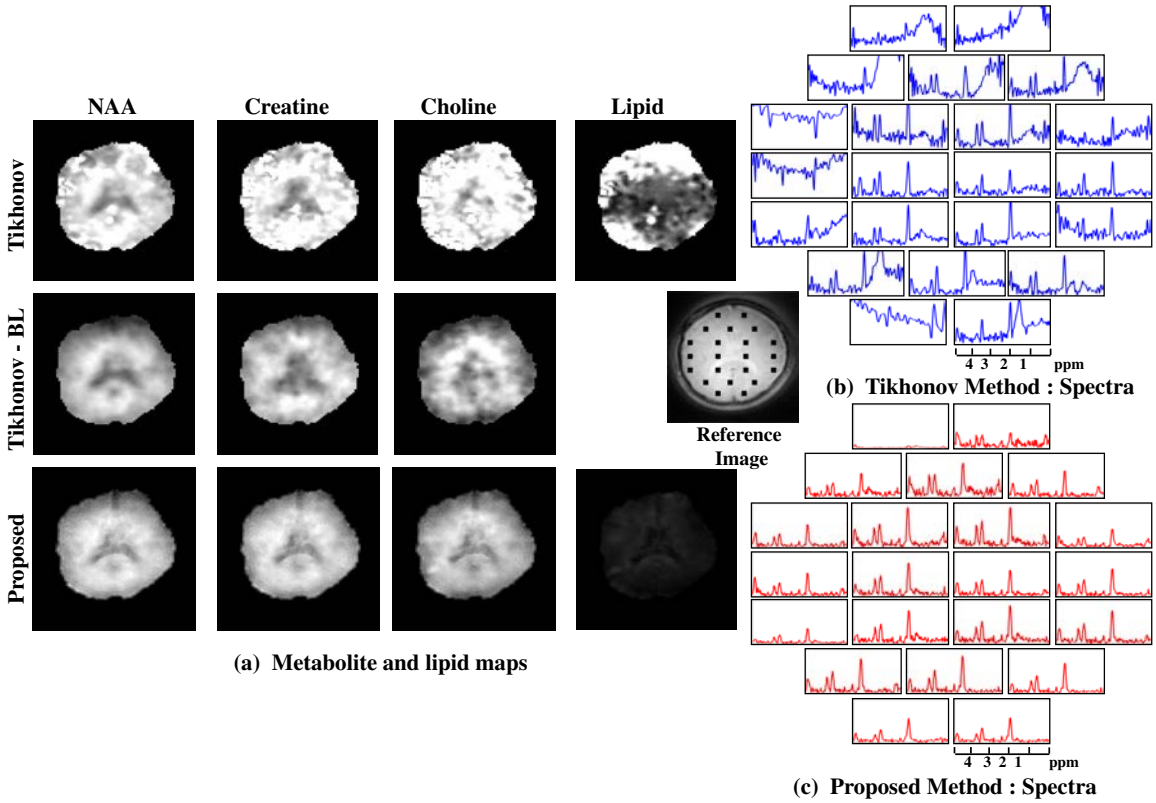

Figure 2.6: *In-vivo* experiments with lipid suppression: The metabolite maps and the lipid maps are shown for the Tikhonov method and proposed method in (a).The metabolite maps obtained from the Tikhonov method with residual lipids removed by polynomial baseline (BL) removal is also shown. Spectra from the locations marked in the reference image are shown in (b) for the Tikhonov method (in blue) and in (c) for the proposed method (in red).

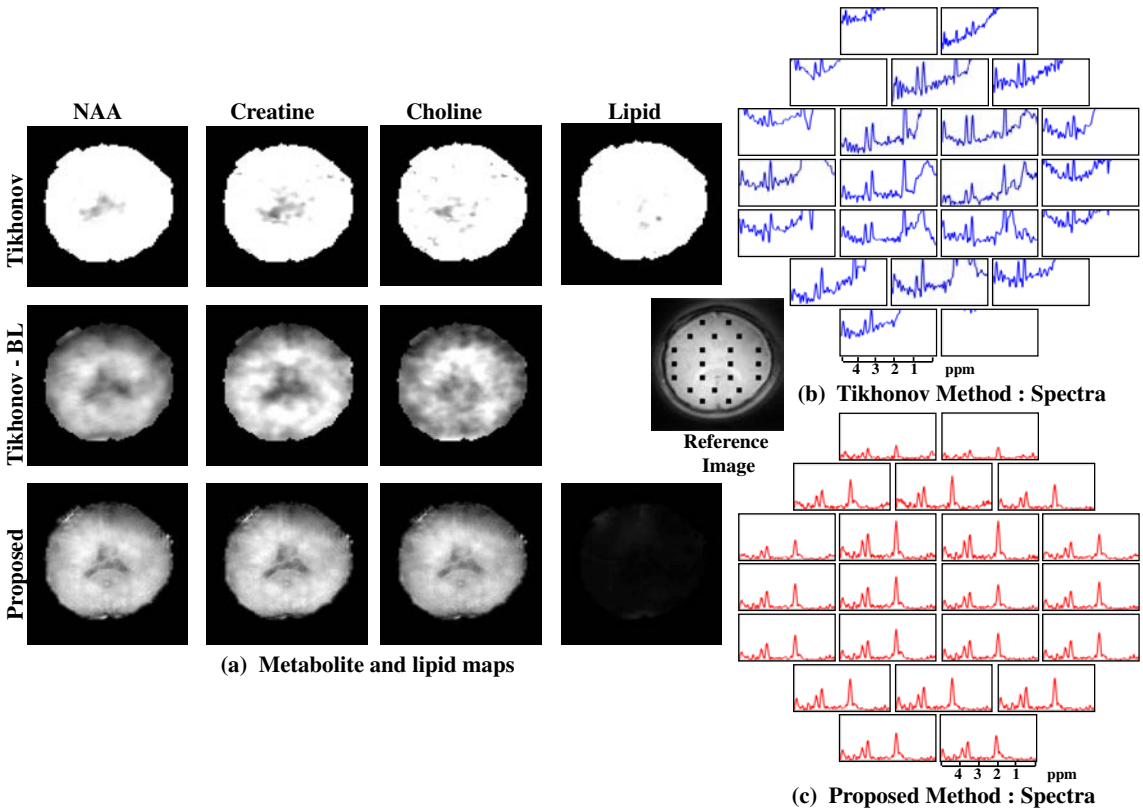

Figure 2.7: *In-vivo* experiments without lipid supression: The metabolite maps and the lipid maps are shown for the Tikhonov method and proposed method in (a).The metabolite maps obtained from the Tikhonov method with residual lipids removed by polynomial baseline (BL) removal is also shown. Spectra from the locations marked in the reference image are shown in (b) for the Tikhonov method (in blue) and in (c) for the proposed method (in red).

present and spatial blurring can be observed . The proposed method is seen to recover the data with minimal lipid leakage artifacts. The spectra at the pixels marked in the reference image are shown in Fig. 7(b) & (c) for Tikhonov LR and proposed method respectively.

The comparison of, the spectra obtained by Tikhonov method for the lipid suppressed data after baseline suppression, and the proposed method is shown in Fig. 8.

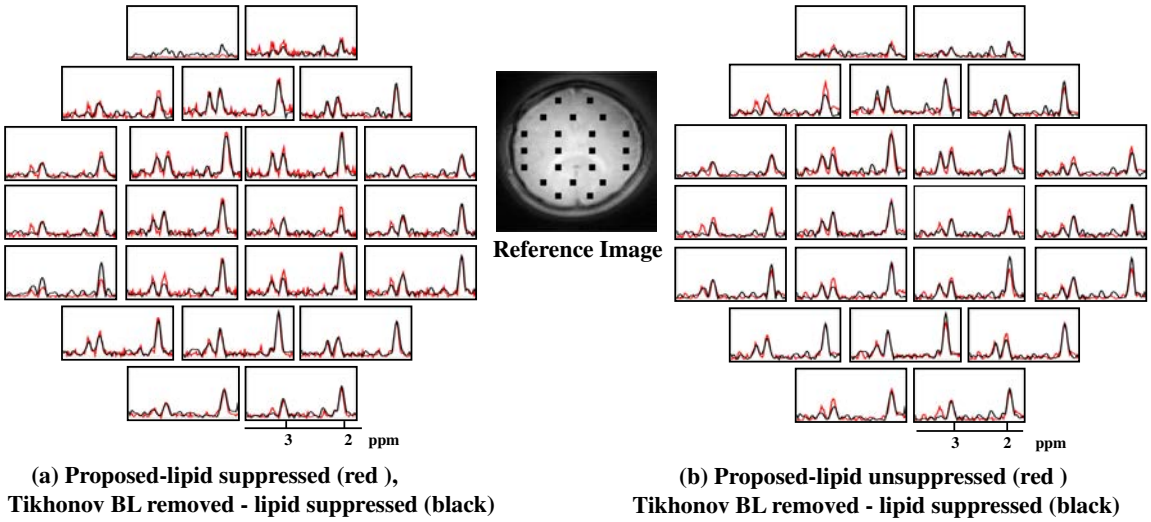

Figure 2.8: Comparison of spectra from proposed method with and without lipid suppression against Tikhonov method with lipid suppression: (a) Spectra recovered by the proposed method from lipid suppressed data is plotted in red (spectra in Fig. 2.6.c in the range 4-1.7 ppm), while the spectra recovered by Tikhonov method from lipid suppressed data after baseline (BL) removal (of spectra in Fig. 2.6.b) are plotted in black. (b) Spectra at the locations marked in the reference image recovered by the proposed method from lipid unsuppressed data (spectra in Fig. 2.7.c in the range 4-1.7 ppm) is plotted in red, while the spectra recovered by Tikhonov method from lipid suppressed data after baseline (BL) removal (of spectra in Fig. 2.6.b) are plotted over in back. We emphasize that the black spectra (Tikhonov) in both plots are derived from lipid suppressed data. These plots show that the proposed method can enable the recovery from lipid unsuppressed data.

The spectra recovered by the proposed method for the lipid suppressed case are

plotted in red, after truncation at 1.7 ppm in Fig. 8(a), whereas the Tikhonov method results after baseline removal for the lipid suppressed data are plotted in black. Fig. 8(b) shows the comparison of the proposed method for the lipid unsuppressed data (in red) with Tikhonov method results for lipid suppressed data after baseline removal (in black). The spectral lineshapes are similar in both cases and also the spectral quality of the proposed method is comparable for both lipid suppressed and unsuppressed case.

2.5 Discussion

We introduced a novel compartmentalized low-rank based algorithm and a spiral dual-density MRSI sequence for reconstruction of high resolution MRSI reconstruction without lipid suppression. The proposed method enables the recovery of high resolution metabolite maps with minimal lipid leakage artifacts from short echo time acquisitions even in the absence of lipid suppression. This approach may be useful in three dimensional acquisitions, when the placement of OVS bands for lipid suppression is difficult. The ability of the scheme to work in short echo time may improve the detection of metabolites with spin-coupled system and also results in improved SNR.

Low rank methods have been used in MRSI by several groups for denoising [85] and reconstruction [58, 63, 64, 69, 75]. The direct use of global low-rank methods as in [58] may be challenging in our lipid unsuppressed setting. In the dual-density sampling setting we would like to constrain the low SNR metabolite regions much more than the high SNR lipid signals; a single subspace would be dominated by lipid basis functions due to the huge dynamic range between the lipid and metabolite signals. The proposed single step compartmentalized low-rank algorithm shares conceptual similarities to two step low-rank methods in [63, 64, 75]. These methods estimate the basis functions from low spatial resolution data, which are separated into metabolite and lipid basis using spatial and spectral prior information in the first step; these basis

sets are used for the recovery of the signals from high-resolution measurements in the second step. While good recovery is demonstrated using OVS and long TEs to reduce lipid signals, the direct use of these methods in our setting (no lipid suppression and short TE) may be challenging. Specifically, good separation of the metabolite and lipid basis functions from low spatial resolution data may be difficult when no lipid suppression is used; lipid signals may be present in all spatial regions, which will limit the utility of spatial priors. In addition, these methods may also be vulnerable to large field inhomogeneity induced variations, which are usually present in the extra-cranial regions. Specifically, the field map induced spectral shifts will translate to spectral distortions of lipid and metabolite signals, which may make it difficult to separate the lipid and metabolite basis sets using spectral prior information. In contrast to the above methods, the proposed method aims to estimate the basis functions from all the available k-space encodes using the orthogonality between the metabolite and lipid signals. This work is inspired by the use of orthogonality constraints introduced in [13], where the lipid and metabolite signals are shown to have strikingly different spectral signatures (e.g. metabolite signals are highly localized in frequency, while the lipid signals are very broad due to the fast T_2 decay). The distinction between these signals are preserved even in the presence of field inhomogeneities. The use of these priors, along with field inhomogeneity compensation, enables the recovery of metabolite data with minimal leakage, even in the absence of lipid suppression. No other algorithm is capable of recovering the MRSI signals without any lipid suppression schemes to the best of our knowledge.

The dual-density acquisition method is inspired by [2, 100]. This approach capitalizes the considerably higher signal intensity of lipids than the metabolites. The variable density spiral approach is more reliable than dual-density Cartesian scans, which requires sophisticated data registration and data mismatch correction to combine data from different acquisitions [30, 63, 64, 75, 82]. Our future work will include

the use of only a subset of the 288 interleaves, which corresponds to Nyquist sampling of lower k-space regions and subsampling of higher k-space regions. We expect the compartmentalized low-rank method, bolstered with parallel imaging [68, 109], to provide good recovery even in this setting. The efficiency of our current sequence may be improved by using more spectral interleaves. Specifically, around 40% of the acquisition time is now devoted for ramping down the spiral gradients and rewinders. The use of spectral interleaves may enable us to increase the efficiency, which will translate to improved SNR efficiency.

2.6 Conclusion

We introduce a novel compartmentalized low-rank algorithm with orthogonality constraint which enables reconstruction of high resolution metabolite maps without the use of any lipid suppression methods. The proposed method is effective at short TE (55 ms) acquisitions also. Also an efficient dual-density data acquisition method using variable density spirals has been introduced to achieve high resolution lipid estimates in a feasible scan time.

CHAPTER 3
DENOISING AND DEINTERLEAVING OF EPSI DATA USING STRUCTURED LOW-RANK MATRIX RECOVERY

3.1 Introduction

Echo-planar spectroscopic imaging (EPSI) [12, 33, 95, 96], which relies on echo-planar readouts to simultaneously encode one spectral and one spatial dimension, is a popular approach for rapid MRSI. Spectral interleaving is often used to simultaneously achieve high spectral and spatial resolution, which is an important need on high field systems that offer higher signal to noise ratio and higher chemical shift dispersion. Specifically, multiple datasets acquired with low temporal sampling rate, but with different temporal shifts between the readouts; the interleaves are later interlaced to construct the final spectrum. A challenge in this approach is the phase inconsistencies between the interleaves, resulting from timing errors in the applied gradient trains, drifts in the magnetic field, and field inhomogeneity distortions. These errors often manifest as spurious Nyquist ghost peaks in the spectral domain (see Fig. 3.1 for details); the associated line-shape variations and baseline fluctuations often make the quantification of relatively weak metabolites rather challenging. We introduce a novel correction strategy, which exploits the annihilation relations resulting from phase relations between the interleaves and linear predictability of exponential signals.

Shortening scan time has been a prime focus of magnetic spectroscopic imaging (MRSI) research [9,10]. EPSI [31] achieves accelerated data acquisition by using echo-planar readouts to simultaneously encode one spectral and one spatial dimension in one acquisition. This approach offers a speed up that is equal to number of points along one spatial dimension. However, it imposes high demands on the gradient system to maintain sufficient spectral resolution on high field systems that have greater spectral dispersion. A common practice to achieving sufficient spectral resolution is spectral interleaving, where the readouts are delayed in time for each spectral inter-

leave. The data from multiple interleaves are upsampled and interlaced to form the final spectrum. A challenge associated with this strategy is the phase inconsistencies between interleaves, resulting from timing errors in the applied gradient trains, drifts in the magnetic field, and dependence on field inhomogeneity distortions. This problem is similar to Nyquist ghosting artifacts in echo-planar imaging (EPI), which manifests as Nyquist ghosts in the phase encoding dimension. In EPSI acquisitions, the phase inconsistencies manifest as spurious peaks in the spectra, which often makes the interpretation of the data challenging. Specifically, the proximity of a spurious peak from a strong metabolite may result in lineshape changes, affecting the accurate quantification of a relatively weak metabolite. Likewise, the intensity of the true peak may also be reduced since the energy is split between the true peak and ghost peak.

Several methods have been developed for the reduction of spectral ghosts in EPSI data. The conventional approach processes the odd and even echoes separately [101] reducing the spectral bandwidth by half; hence is not an option for high field scanners. Methods relying on theoretical estimates of k-t space trajectory such as the interlaced Fourier transform method [81] or the Fourier shift method [45] ignore the phase distortion between the echos. Echo misalignment [81,101] correction has shown good potential in the reduction of spurious peaks, contingent to accurate estimation of k-t space trajectory that is often not practical in the presence of drifts and B_0 inhomogeneity. Another popular method is to estimate the phase inconsistencies from the center of k-space and correct for the misalignment between the echoes [26] during data processing. Even though this method has shown promise in fat-water imaging, its utility for low-intensity metabolites is yet to be seen.

We introduce a novel reconstruction method for EPSI data which does not depend on accurate estimates of phase inconsistencies or k-t space trajectory to suppress the spectral ghosts. We exploit the annihilation relations in spectrally interleaved EPSI data resulting from the linear predictability of exponential signals and phase relations

between the interleaves. We pose the problem as a recovery of two signals at each pixel, corresponding to the odd and even interleaves. The proposed framework is inspired by our MUSSELS strategy used in multishot EPI acquisitions [76], which is conceptually similiar to [66, 73]. Unlike these methods [66, 73, 76] that rely on coil sensitivity information or signal smoothness to avoid the trivial solution resulting from uniform undersampling, we rely on the annihilation property due to linear predictability of the exponentials. We construct a block Hankel matrix, whose entries correspond to the two echoes, that capture the annihilation relations in a compact way; the annihilation relations translate to a low-rank block Hankel matrix, which we recover from undersampled measurements using structured nuclear norm minimization.

We demonstrate the results of the proposed method using several datasets. High resolution ^{13}C MRSI data of mouse kidney acquired at 9.4T using bipolar EPSI readout gradients is used for the first experiment. The proposed methods show improvement in the signal of Pyruvate maps due to recovery of real spectral peaks and reduction of spurious peaks leading from combination of odd and even echoes. The second and third set of experiments were conducted on high resolution ^{1}H *in-vivo* MRSI data collected at 3T using flyback trajectories. The two datasets were collected at different spatial resolution and spectral bandwidth. The proposed method show increased SNR for the metabolite maps and removal of spurious signals.

3.2 Theory

3.3 Background

We assume that the true spectrum at a specified pixel $\mathbf{r}$ as a multi-exponential model:

$$\rho[\mathbf{r}, n] = \sum_{k=1}^{K} c_k[\mathbf{r}] \ \ (\nu_k)^n \, ; \quad n = 0, .., N-1 \tag{3.1}$$

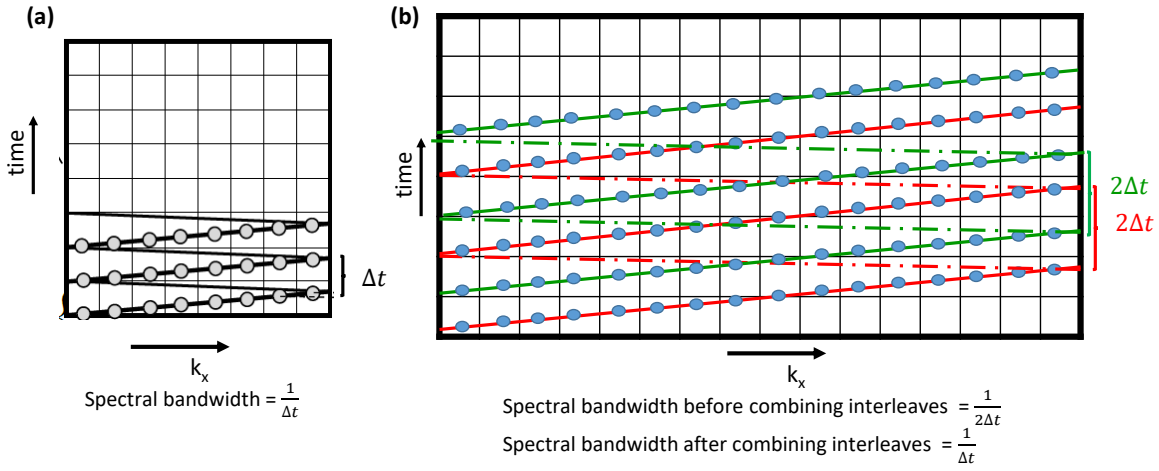

Figure 3.1: Spectral interleaving using flyback EPSI: (a) For each excitation $k_x - t$ space is traversed simultaneously during readout time. This example shows k_x dimension = 8, (b) By doubling the spatial resolution i.e,k_x dimension =16, each interleave takes twice the time which results in half spectral bandwidth. Thus two interleaves are used (red and green) as on combination bandwidth is preserved.

where K is the number of exponentials with parameters

$$\nu_k = \exp\left\{-\left(\frac{1}{T^*_{2,k}} + j2\pi f_k\right)T\right\}, \tag{3.2}$$

and c_k are amplitudes. Here $\left(\frac{1}{T^*_{2,k}} + j2\pi f_k\right)$ are the exponential parameters of the k^{th} exponential and T is the Nyquist sampling interval. We will omit the dependence of the signal on the spatial location for simplicity in the future discussions. The Fourier transform of the signal along n, specified by

$$\hat{\rho}[k] = \sum_{n=1}^{N} \rho[n] \exp\left(-j\frac{2\pi}{N}kn\right) \tag{3.3}$$

will have K peaks at frequencies f_k; the basic goal in MR spectroscopy is to estimate the amplitudes c_k from the data.

Since the bandwidth of the spectrum is too large in high field scanners, it is

often impossible to sample the signal at the Nyquist rate using EPSI. It is a common practice to acquire the data using spectral interleaving, where the signal is sampled twice with a sampling interval of $2T$. Specifically, one would acquire two signals $\rho_{\mathrm{o}}[n]$ and $\rho_{\mathrm{e}}[n]$, where the readout of the odd signal is delayed by T, These signals are later combined as

$$\rho_{\mathrm{combined}}[n] = \begin{cases} \rho_{\mathrm{e}}[n] & \text{if} \quad n \text{ is even} \\ \rho_{\mathrm{o}}[n] & \text{if} \quad n \text{ is odd} \end{cases} \tag{3.4}$$

Unfortunately, ρ_{e} and ρ_{o} are acquired at two different acquisitions and hence would differ in terms of a phase distortion. The distortion is often a complex function of the readout delay T and the field inhomogeneity at the spatial location $\mathbf{r}$. Hence, the combined signal (3.4) often suffers from spectral ghosts, shifted from the original point by N/2 spectral points; the distribution of the amplitudes to the two peaks is dependent on the phase distortion. A schematic diagram explaining the signal formation is shown in Fig.3.2.

3.4 Methods

We introduce an algorithm for the removal of spurious peaks as well as the denoising of spectroscopic MRI data. The algorithm exploits the annihilation relations induced by the spectral model (3.1) as well as the phase relations in (3.5) & (3.6). We use a lifting strategy, where a structured matrix is formed using the entries of the measured signals ρ_{e} and ρ_{o} to exploit the annihilation relations. The rank of the structured matrix is very low due to the annihilation relations. We use the low-rank property to jointly recover the fully sampled signals $\rho_{\mathrm{e}}[n]; n = 0, .., N-1$ and $\rho_{\mathrm{o}}[n]; n = 0, .., N-1$ from their undersampled measurements.

We model the phase distortions in ρ_{e} and ρ_{o} as convolutions by finite impulse response filters $g_{\mathrm{e}}[n]$ and $g_{\mathrm{o}}[n]$, respectively. Specifically, we assume that

$$\hat{\rho}_{\mathrm{e}}[k] \quad = \quad \hat{\rho}[k] \; \hat{g}_{e}[k] \tag{3.5}$$

$$\hat{\rho}_{\mathrm{o}}[k] \;=\; \hat{\rho}[k]\;\hat{g}_o[k], \tag{3.6}$$

where the signals $g_e[k]$ and $g_o[k]$ are specified by

$$g[k] \;=\; \sum_{p=-M}^{M} c[k] \exp\left(-j\frac{2\pi pk}{N}\right) \tag{3.7}$$

Note that the above model can easily account for differences in phases and differences in frequencies in a small range determined by T, between the two acquisitions.

3.4.1 Annihilation Relations Induced by Exponential Model

Exponential signals in (3.1) satisfy an annihilation relation [5, 106]:

$$\rho[n] * h[n] = 0, \tag{3.8}$$

where h is the FIR filter of the form

$$h(z) = \prod_{i=1}^{K} \left(1 - \nu_k z^{-1}\right). \tag{3.9}$$

Since $\rho_{\mathrm{e}}(z) = \rho(z)h_e(z)$ and $\rho_{\mathrm{o}} = \rho(z)h_o(z)$, both of these signals also satisfy (3.8) with the same filter. The convolution relation in (3.8) can be expressed as in the matrix form as $\mathbf{Q}_e\mathbf{h} = 0$ and $\mathbf{Q}_o\mathbf{h} = 0$, where $\mathbf{Q}_e$ and $\mathbf{Q}_o$ are $(N - K + 1) \times K$ dimensional Hankel matrices formed from the samples of ρ_o and ρ_e, respectively. In reality, the number of exponentials K is unknown, when one can overestimate it as P. In this case, any filter specified by $h_n(z) = h(z)\eta(z)$ such that h_n is a P tap filter also annihilates the signal. Since one can find $P-K$ linearly independent filters $\eta(z)$, the rank of the $(N - P + 1) \times P$ dimensional matrices $\mathbf{Q}_o$ and $\mathbf{Q}_e$ can be shown to be equal to $K - 1$ (see [5] for details).

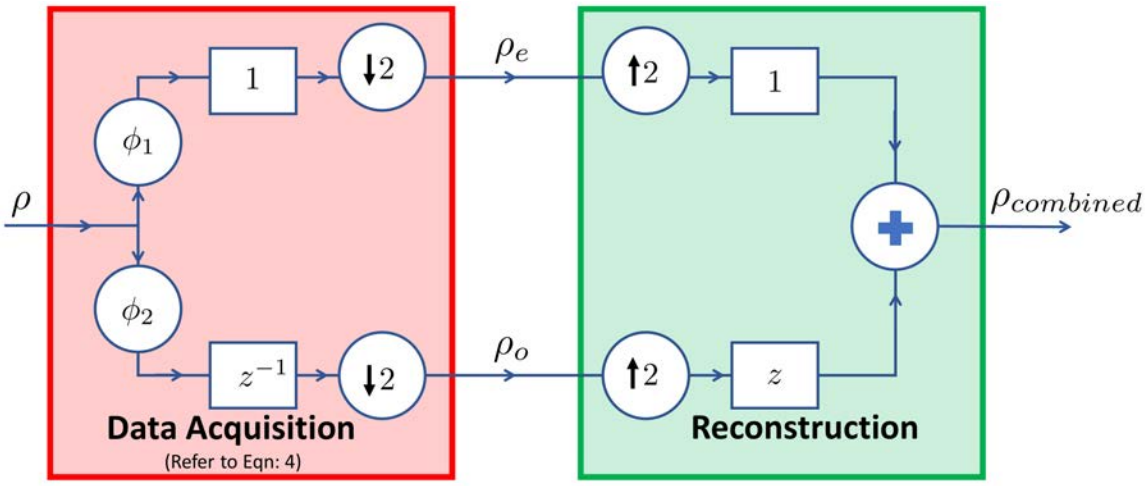

Figure 3.2: The FID at each pixel *rho* are corrupted by different phase distortion functions ϕ_1 & ϕ_2 before combining the odd (ρ_o) and even (ρ_e) as shown in the data acquisition block as described in Eqn:3.4. Standard schemes form the interleaved signal $\rho_{combined}$ as shown in the reconstruction block. We propose to replace the reconstruction by Eqn: 3.13.

3.4.2 Annihilation Property Induced by Phase Relations

The model specified by (3.6) and (3.5) implies that there exists annihilation relations between the two signals

$$\rho_{\mathrm{e}}[n] * g_o[n] - \rho_{\mathrm{e}}[n] * g_e[n] = 0. \tag{3.10}$$

This annihilation relation can be represented in the matrix form as

$$\underbrace{[\mathbf{Q}_e, \mathbf{Q}_{\mathrm{o}}]}_{\mathbf{Q}} \begin{bmatrix} \mathbf{g}_o \\ -\mathbf{g}_e \end{bmatrix} = \mathbf{0}, \tag{3.11}$$

where $\mathbf{Q}_{\mathrm{o}} = \mathcal{T}(\rho_{\mathrm{o}})$ and $\mathbf{Q}_e = \mathcal{T}(\rho_{\mathrm{e}})$ are $(N - M + 1) \times M$ dimensional convolution (Hankel) matrices obtained from the samples $\rho_{\mathrm{o}}[n]$ and $\rho_{\mathrm{e}}[n]$, respectively.

In reality, one often does not know the precise value of M needed to model the phase distortion; we overestimate the support to $P \geq M$. In this case, there are multiple annihilation relations, involving filters $\tilde{g}_{\mathrm{o}}(z) = g_{\mathrm{o}}(z)\gamma(z)$ and $\tilde{g}_{\mathrm{e}}(z) = g_{\mathrm{e}}(z)\gamma(z)$,

where $\gamma(z)$ is an arbitrary filter such that $\tilde{h}_{\mathrm{o}}(z)$ and $\tilde{h}_{\mathrm{e}}(z)$ are still support limited within M. This implies that the matrix $\mathbf{H}$ is low-rank.

We note that the combined lifting will benefit from both the exponential structure and phase relations. Specifically, we have

$$\underbrace{[\mathbf{Q}_e, \mathbf{Q}_{\mathrm{o}}]}_{\mathbf{Q}} \begin{bmatrix} \mathbf{g}_o * \boldsymbol{\gamma} & \mathbf{h} * \boldsymbol{\eta} & \mathbf{0} \\ -\mathbf{g}_e * \boldsymbol{\gamma} & \mathbf{0} & \mathbf{h} * \boldsymbol{\eta} \end{bmatrix} = \mathbf{0}, \tag{3.12}$$

Both the annihilation relations together result in a matrix with small rank.

3.4.3 Proposed Structured Low-Rank Algorithm

We use the low-rank structure of $\mathbf{Q}$ to recover the two signals μ_{o} and μ_{e} from their undersampled measurements:

$$\begin{aligned} \{\boldsymbol{\mu}_o, \boldsymbol{\mu}_e\} \;=\; & \arg\min_{\boldsymbol{\mu}_o, \boldsymbol{\mu}_e} \|\mathcal{A}_o(\boldsymbol{\mu}_o) - \boldsymbol{\rho}_o\|^2 + \|\mathcal{A}_e(\boldsymbol{\mu}_o) - \boldsymbol{\rho}_e\|^2 + \lambda_1 \sum_{i=1}^{N_{\mathrm{pixels}}} \| \underbrace{\left[\mathcal{T}(\boldsymbol{\mu}_o^{(i)}), \mathcal{T}(\boldsymbol{\mu}_e^{(i)})\right]}_{\mathbf{Q}} \|_* \\ & + \lambda_2 \left[\| \underbrace{\boldsymbol{\mu}_o}_{\text{Casortai low-rank}} \|_* + \| \boldsymbol{\mu}_o \|_* \right] \end{aligned} \tag{3.13}$$

where $\mathcal{A}_o$ and $\mathcal{A}_e$ are undersampling operators corresponding to $\boldsymbol{\rho}_o$ and $\boldsymbol{\rho}_e$, respectively. We use an iteratively reweighted nuclear norm minimization algorithm to minimize the above cost function and recover the signals.

The third term synergistically uses the spectral & phase-induced annihilation relations, enables the removal of phase errors and provides spectral denoising. The combination of priors also eliminates the trivial solution introduced by structured sampling [73]. The last term is the sum of nuclear norms of the Casoratti matrices $\boldsymbol{\mu}_o$ and $\boldsymbol{\mu}_e$, which facilitates in further spatial denoising high resolution MRSI data.

Post recovery, we use root mean square of $\boldsymbol{\mu}_o$ & $\boldsymbol{\mu}_o$ as the recovered signal. Since exponential signals with fewer exponential parameters are associated with lower rank,

the proposed formulation performs simultaneous denoising and deinterleaving.

The periodic undersampling pattern that results from interleaved sampling may result in a trivial solution, if the spectral annihilation relations are not exploited [73]. Specifically, the trivial solution $\mu_{\mathrm{o}} = \rho_{\mathrm{combined}} = \mu_{\mathrm{e}}$ will satisfy the data consistency relations and the trivial annihilation relation $\mu_{\mathrm{e}}[n] * \delta[n] - \mu_{\mathrm{e}}[n] * \delta[n] = 0$, resulting in a matrix of rank P. However, when the signal follow a multiexponential model as in (3.1), we observe that the trivial solution has $2K$ (double the number of exponential parameters), when compared to the true solution due to aliasing. This shows that the trivial solution is not the one that satisfies the data consistency constraints and yield the minimum rank of $\mathbf{Q}$. We study the impact of the different priors in Fig. 3.3, where we set $P = 15$. In the top row, we study the effect of the phase relations alone. We consider a random signal that does not follow a multipeak model, while ρ_e and ρ_o are related to the random signal by a phase term. In this case, $\mathbf{Q}_e$ and $\mathbf{Q}_o$ are full rank matrices (rank 15 each). The presence of the phase relations (3.11) results in 15 nullspace vectors, and hence the combined matrix $\mathbf{Q}$ is of rank $P = 15$. In this case, we observe that the trivial solution obtained by interleaving also results in 15 null space vectors and hence the corresponding $\mathbf{Q}$ is also of rank $P = 15$. The structured low-rank method fails in this case.

In the second row, we study the impact of the the linear predictability alone. We consider two four peak signals ρ_e and ρ_o that are not related by a phase term. The peaks are at different locations. In this case, $\mathbf{Q}_e$ and $\mathbf{Q}_o$ are of rank $k = 4$ each. The concatenated matrix does not have any additional null space filters since there are no phase relations; the rank of the true Q matrix $2K = 8$, which is equal to the sum of the ranks of $\mathbf{Q}_e$ and $\mathbf{Q}_o$. The zero filled signals have eight peaks each and does not satisfy any null space relations, thus resulting in a rank of $P = 15$. The combined signal has 16 peaks each, but satisfies 15 null space relations, resulting in a rank of $P = 15$. The recovery fails in this case as well.

In the third row, we study the case with both linear predictability and phase relation. In this case, $\mathbf{Q}_e$ and $\mathbf{Q}_o$ are of rank $k = 4$ each, with the null spaces overlapping. The presence of the phase induced annihilation relations result in null space vectors, but several of them are linearly related. The rank of $\mathbf{Q}$ is equal to K in this case, which is much smaller than that of the interleaved signal as well as the zero filled case. In this case, we observe that the nuclear norm recovery succeeds, thus enabling the recovery of the signals. These experiments show that both linear predictability and phase relations are required for the successful recovery of the spectra.

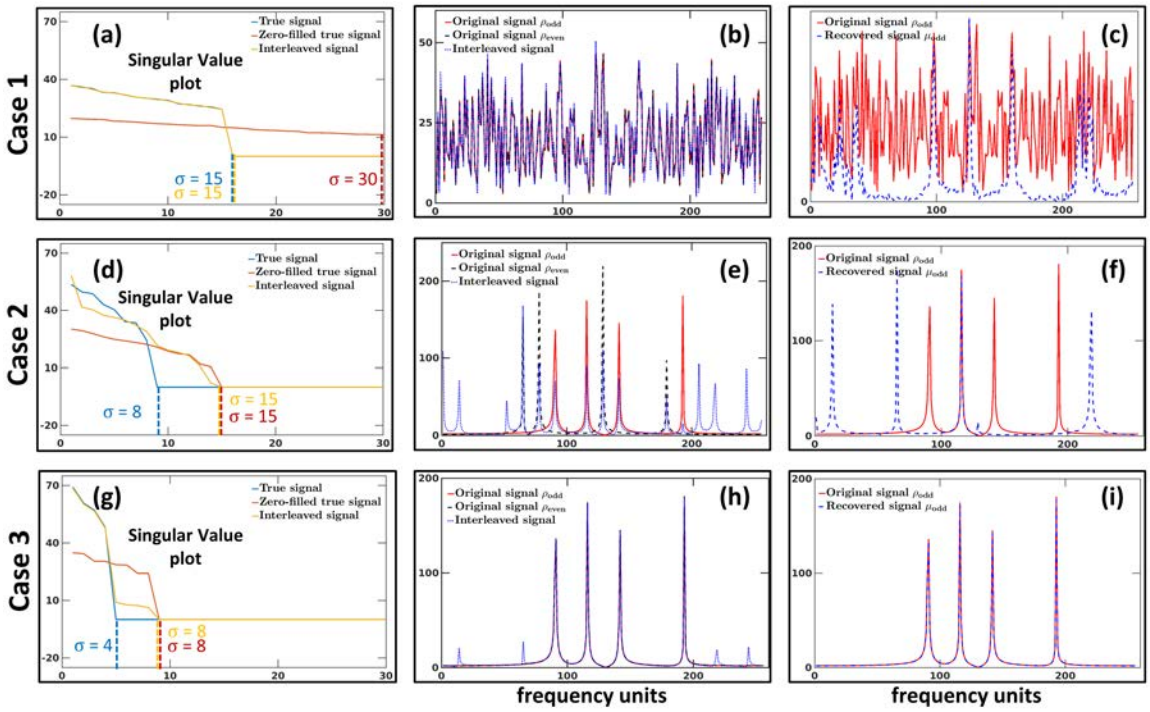

Figure 3.3: Simulated Experiment: We study 3 cases to understand the effect of annihilation priors. Case1 : Random signal that does not follow a multipeak model related by phase term. This case fails as the true rank is too high. effect of annihilation priors. Case2 : Two multipeak signals which are not related by phase term. This only exploits linear predictability and does not have enough null space vectors and thus fails. Case 3: Multipeak model with phase relation. This case exploits both the annihilation relations and has enough null space vectors to achieve recovery.

3.5 Experimental Methods

In this study we have used three in-vivo datasets to validate the proposed algorithm. We start with a simpler MRSI dataset of ^{13}C Hyperpolarized mouse kidney which has decent SNR for the main metabolite peak of pyruvate. We then extend our studies to ^{1}H MRSI subject scans which are highly SNR deprived and has adverse effects arising from spurious peak formation. We also tested our algorithm on EPSI using both bipolar readout gradients (^{13}C Hyperpolarized data) and flyback trajectories (^{1}H MRSI data).

Dataset 1: Hyperpolarized 13C mouse kidney MRSI All experiments were performed using 9.4T small animal imaging scanner (Bruker BioSpin MRI GmbH, Germany) equipped with ^{1}H-^{13}C dual-tuned mouse volume Tx/Rx coil. [1-13C] pyruvic acid doped with 15mM Trityl radical and 1.5M Dotarem was polarized for 1 hour using HyperSense DNP polarizer (Oxford Instruments, Oxford, UK). Hyperpolarized sample was dissolved with Tris/EDTA-NaOH solution, and 350ul of pyruvate was injected into Balb/c mouse through tail vein catheter over duration of 5s. 3-mm thickness of axial-oriented slice containing mouse kidney was selected, and the scan was started at 5s after injection of the pyruvate. All procedures of the animal experiments were approved by the local animal care and use committee. Echo-Planar Spectroscopic Imaging (EPSI) with bipolar readout gradient (called as D2 dataset, sparse sampling in spectral domain). Field map was also acquired for B0 inhomogeneity compensation. This data was collected at Yonsei Univeristy, South Korea.

Dataset 2: 1H MRSI in-vivo experiments at resolution 32×32 A volunteer was scanned with a GE MR750W 3T scanner at the University of Iowa using a 32-channel head coil under a protocol approved by the Institutional Review Board (IRB) of the University of Iowa. Single slice proton MRSI data were collected from one healthy volunteer, after receiving informed consent. An oblique axial slice above

the ventricles was acquired with FOV = $220 \times 220\ mm^2$ and a slice thickness = 10 mm. PRESS box based excitation is used to collect data using flyback EPSI trajectories. The center of the brain is excited such that signals from lipid layer are avoided. A matrix size of 32×32 is collected with 512 spectral points using 2 spectral interleaves resulting in a effective bandwidth of 1000 Hz. The TR/TE for the dataset is 1000/30 ms. 8 averages are collected resulting in total scan time of 8 mins. The residual water was removed in the post-processing stage.

Dataset 3: 1H MRSI in-vivo experiments at resolution 64×64 Another dataset is collected similar to Dataset 2. A matrix size of 64×64 is collected with 256 spectral points using 2 spectral interleaves resulting in a effective bandwidth of 595 Hz. The TR/TE for the dataset is 1000/30 ms. 8 averages are collected resulting in total scan time of 16 mins. The residual water was removed in the post-processing stage.

Reconstructed Data compared with Phase Correction Method We compared the reconstructed results with popular phase correction methods. An estimate of the phase inconsistency is generated from the data and is used to correct for the spurious peaks. However this method does not achieve denoising which is unavoidable for high resolution EPSI.

3.6 Results

We study the performance of the proposed algorithm across three different datasets and especially one at high field strength where increased spectral dispersion demands interleaving. We also test the other aspect of EPSI which is low SNR at higher resolution which makes it challenging.

We report our observation for the first set of experiments on ^{13}C mouse kidney dataset in Fig. 3.4. The proposed method and the classical phase correction methods

are compared. In this dataset we are concerned about the Pyruvate signals at high resolution. The spurious peak map, which corresponds to the intensity distribution at the frame at which the spurious peak of Pyruvate appears is shown for the uncorrected, phase corrected and proposed method in (b) -(d) respectively. It is clear that the proposed method shows improved performance in removing the spurious peaks which is exemplified by the reduced intensities in that frame whereas phase correction method ks unable to completely remove it. The Pyruvate metabolite map for the three methods in (f)-(h), on the other hand, show improved SNR for the proposed method as shown by the arrows in (h). For a better demonstration of the improved Pyruvate SNR, we report percentage intensity increase map in (e) which is achieved by calculating $\frac{\|Pyruvate_{proposed} - Pyruvate_{uncorrected}\|}{\|Pyruvate_{uncorrected}\|} \times 100$. It shows upto 70 % increase in intensities, especially in the edges of the kidney.

In Fig. 3.5 the spectra at three reference pixels (reference image in Fig.4(a)) are plotted for the three methods. It can be observed that the phase correction method is successful in removing spurious peaks from most pixels but has suboptimal performance for the renal medulla pixel. Also it does not provide any denoising. The proposed method on the other hand removes all spurious peaks in addition to denoising the spectra which is neccessary for high resolution EPSI data. For this experiment only Toeplitz low rank structure was able to provide enough denosing and thus Casorati constraint was not applied.

It should also be noted that the increased SNR is because the signal energy is restored in the original peak location by the proposed method which otherwise is split between real and spurious peak in the uncorrected data. This also shows the application of the proposed method at high field strength magnets.

We study the performance of the proposed method on a *in-vivo* 1H MRSI dataset collected at a resolution of 32x32. We do not compare the performance of the proposed method with phase correction method for the ^1H datasests as it performs

sub-optimally for the relatively higher quality ^{13}C dataset. The major challenges of this dataset include low SNR and the huge spurious peak of water which is comparable or more powerful than the metabolites.

Three metabolite maps corresponding to NAA, Creatine and Choline and the spurious peak frame are reported in Figure. 3.6 in the two rows corresponding to the uncorrected and the proposed method. As can be observed the proposed method shows much improved SNR and preserves high resolution details like better delination of the ventricles. The Creatine and Choline maps for the uncorrected data have poor demarcation of the ventricle details which are preserved by the proposed method. The spurious peak frame of water shows remarkably reduced intensity which denotes better removal of spurious peaks.

Fig. 3.7 shows the spectra corresponding to the reference pixels marked in the image. It is evident that the spectra for the uncorrected data is corrupted by high noise level along with huge spurious peaks especially in the ventricles. The proposed method on the other hand uses two low rank structures, i.e Toeplitz and Casorati resulting in high quality spectra and removal of all spurious peaks.

Our final set of experiments are performed on a very high resolution ^{1}H MRSI dataset of matrix resolution 64×64. This dataset has a bandwidth of 600 Hz, such that the spurious peak of water appears in between NAA and Creatine, thus making the deinterleaving process more challenging.

The three metabolite maps and spurious peak frame shown in Fig. 3.8 for the three methods show high noise levels for the uncorrected data. The spatial details are not resolved without denoising. The proposed method recovers maps with improved SNR and as can be seen very high resolution spatial details are recovered. The spurious peak frame again has reduced intensities for the proposed method showing successful deinterleaving.

The recovered spectra for the the three methods are shown in Fig. 3.9 for the

reference pixels marked in the image. This dataset is particularly challenging because of the very low SNR and the spurious peak formation between NAA and Creatine. The performance of the proposed method is superior to in both the aspects of improving SNR and removing the spurious peaks.

3.7 Conclusion

In this work we proposed a novel algorithm for denoising and deinterleaving of EPSI data without directly estimating phase or relying on theoretical k-space trajectory. We further demonstrated the improvement offered by the proposed method compared to the classical phase correction method. The proposed scheme would be highly beneficial in reconstruction and correction of high-resolution EPSI, especially for the acquisition from high field magnets.

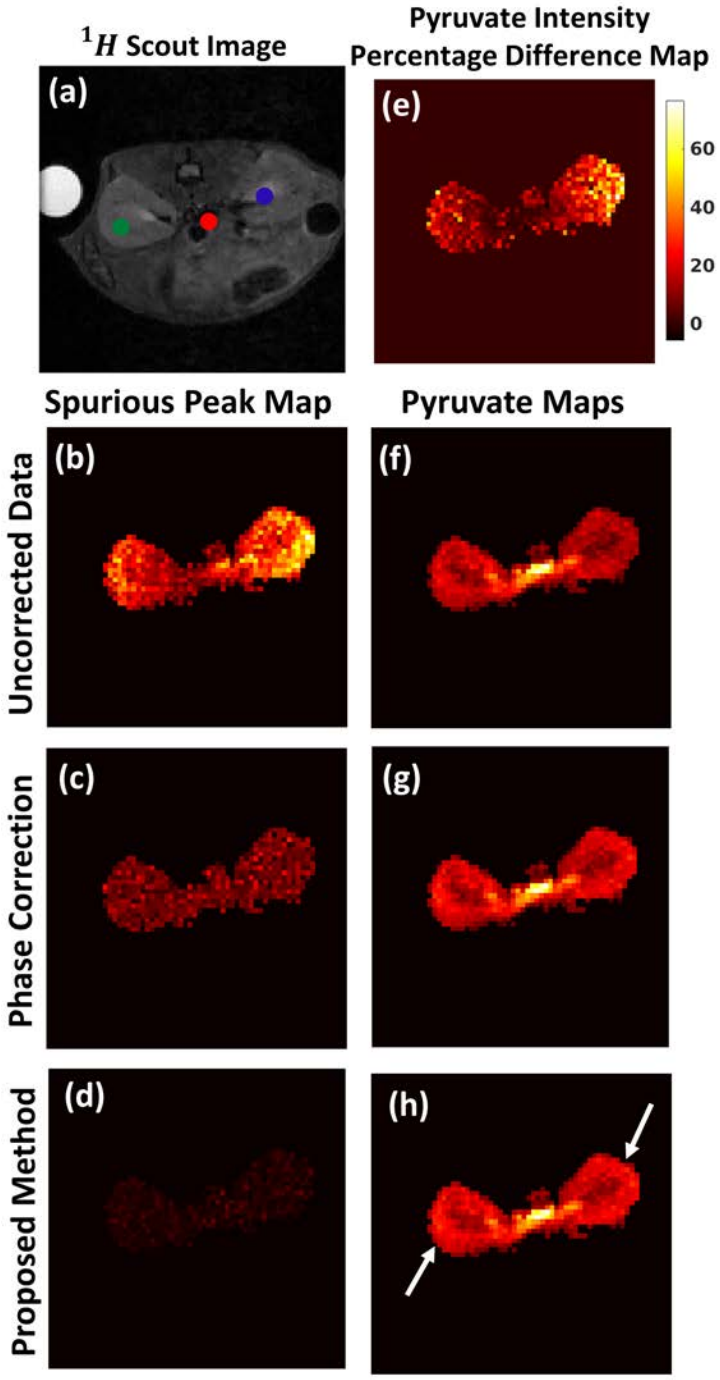

Figure 3.4: Metabolite maps: (a) 1^H reference image of mouse kidney with reference pixels marked in three regions. (b-d) Intensity map at the spurious peak corresponding to Pyruvate and (f-h) Pyruvate maps, for the uncorrected data, phase correction method and proposed method respectively. (e) Map showing percentage increase of signal intensity provided by proposed method compared to uncorrected data. Pixels show upto 70% increase.

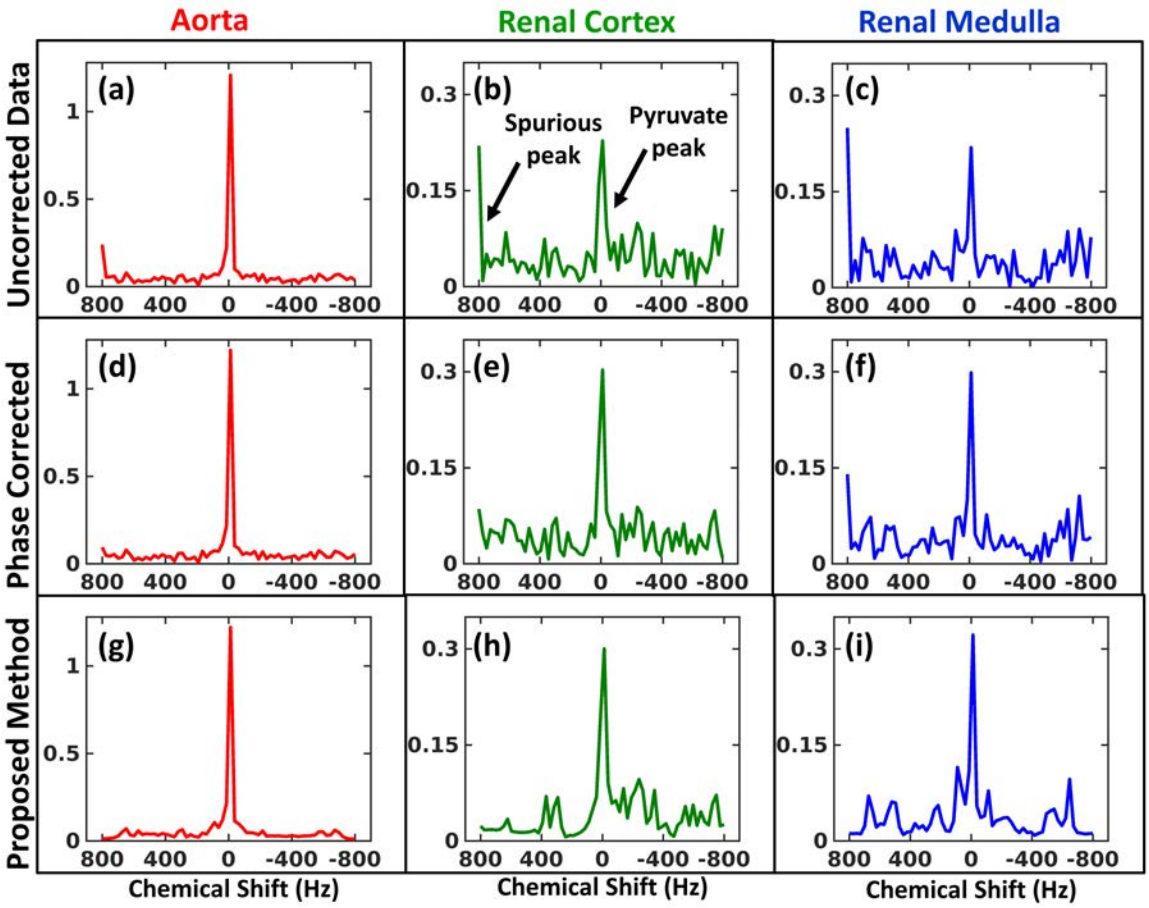

Figure 3.5: Metabolite spectra: First (a-c), second (d-f) and third (g-i) row show the spectra at aorta, renal cortex and renal medulla respectively (refernce pixel location marked in Fig.3.4(a)) for the uncorrected data, phase correction method and the proposed method respectively.

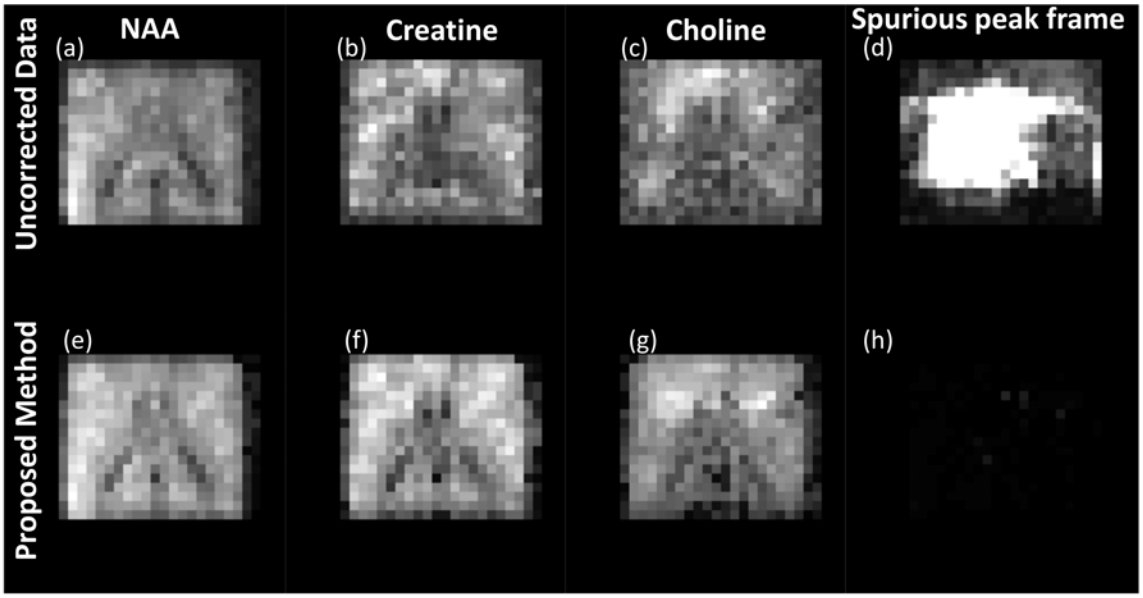

Figure 3.6: Metabolite maps: (a-c) Metabolites maps generated from the uncorrected data by peak integration. The three maps correspond to NAA, Creatine and Choline. (e-g) The maps corresponding to the proposed method showing improved SNR. (d) & (h) correspond to the spurious peak frame for the uncorrected and corrected data respectively.

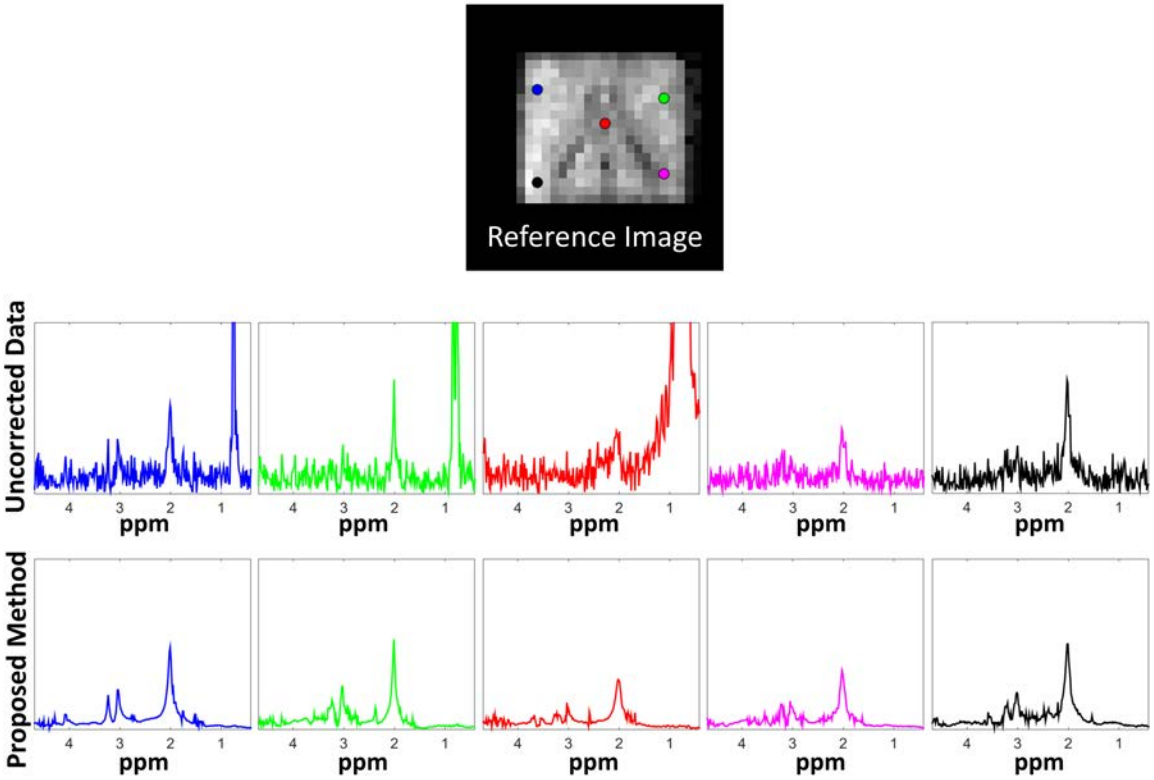

Figure 3.7: Metabolite spectra: First row shows a reference image with the pixel locations for the representative spectra marked. The first row shows the spectra from the uncorrected data which is noisy and has a stromg spurious peak near 1 ppm. The second row showing the spectra from the proposed method show reduced noise and complete removal of spurious peaks.

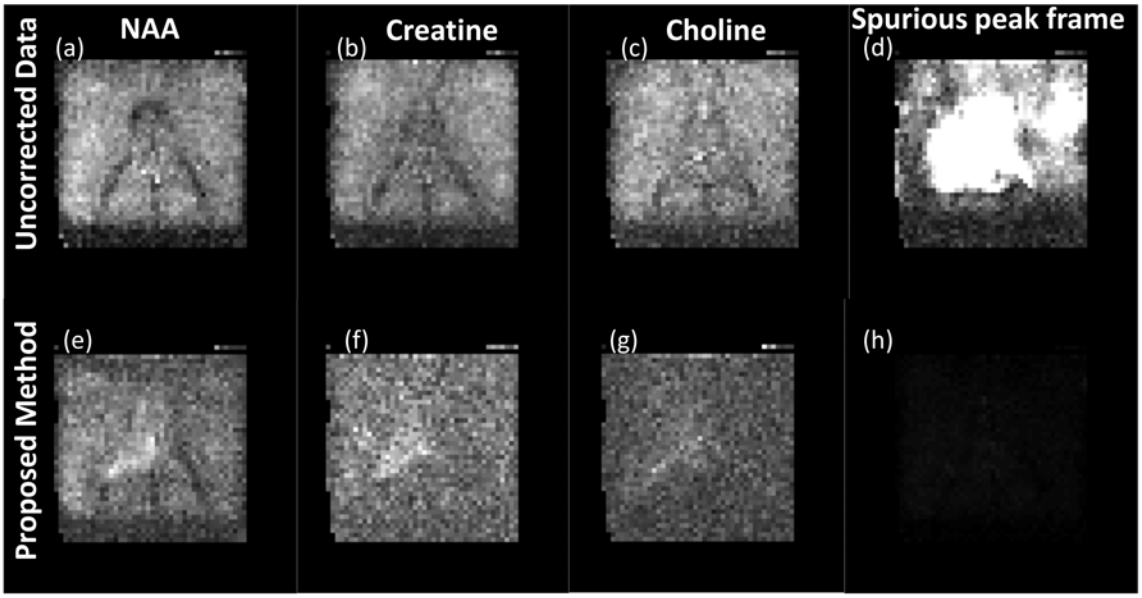

Figure 3.8: Metabolite maps: (a-c) Metabolites maps generated from the uncorrected data by peak integration. The three maps correspond to NAA, Creatine and Choline. (e-g) The maps corresponding to the proposed method showing improved SNR. (d) & (h) correspond to the spurious peak frame for the uncorrected and corrected data respectively.

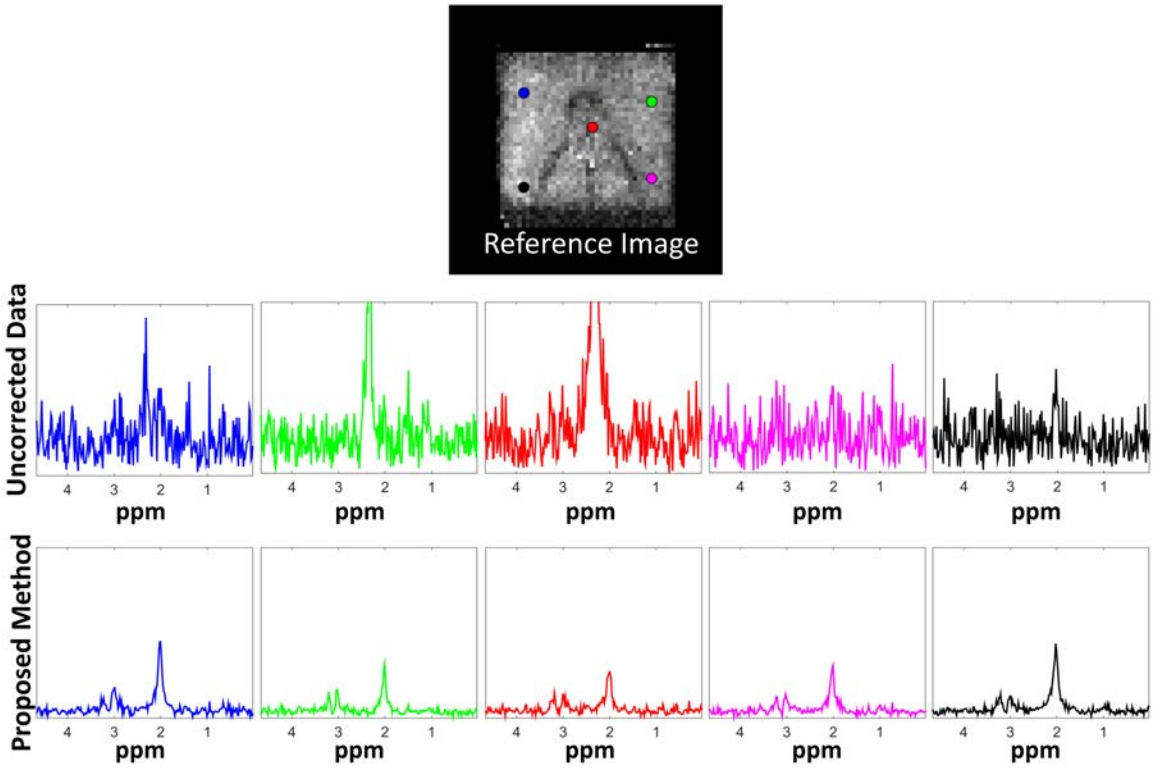

Figure 3.9: Metabolite spectra: First row shows a reference image with the pixel locations for the representative spectra marked. The first row shows the spectra from the uncorrected data which is noisy and has a stromg spurious peak near 2.2 ppm. The second row showing the spectra from the proposed method show reduced noise and complete removal of spurious peaks.

CHAPTER 4
ACCELERATION OF TWO-DIMENSIONAL INFRARED SPECTROS-COPY WHILE PRESERVING LINESHAPES USING GIRAF

4.1 Introduction

Two dimensional infrared (2D IR) spectroscopy is an emerging modality that provides detailed information about the dynamic molecular interactions at femtosecond and picosecond timescales [43, 44]. Its ability to probe the molecular vibrational coupling, vibrational and orientational relaxation, as well as chemical exchange and spectral diffusion makes it an attractive tool to investigate systems from dilute solutions to membranes. However, the main challenge with traditional Fourier scanning methods is long acquisition time, which limits the range of investigations. Some applications require measurement of spectra at multiple waiting times further increasing the measurement time. Recently, we and other groups have investigated the use of compressed sensing (CS) algorithms to minimize the sampling burden [3, 27, 53, 99]. These methods assume the spectrum to be sparse in the Fourier basis (i.e. signal with few spikes in frequency domain) [27] or piece-wise smooth [108] to make the recovery from sub-Nyquist sampled measurements well-posed. However, the vibrational spectra of many systems often consist of broad peaks. Since several spikes are required to represent a single broad peak, the Fourier representation is non sparse; use of sparsity based CS algorithms to recover the signal from highly undersampled data is challenging.

We propose to represent the spectrum as a sparse linear combination of damped exponentials, each with different frequencies and damping coefficients. Note that this is a richer representation than the Fourier basis (undamped exponentials), which is essentially a subspace of our representation. A broad peak can be efficiently approximated as a linear combination of a few damped exponentials (Lorentzians in frequency domain) with possibly different damping rates. The approximation of smooth func-

tions as a linear combination of few Lorentzians is well-studied. For example, several authors have shown that the Voigt lineshape can indeed be well approximated by three or four Lorentzians [78].

We recently introduced an algorithm that uses a dictionary of damped exponentials with continuously varying parameters [5, 88, 89]. This method significantly reduces discretization errors that are prevalent in CS schemes, where discrete dictionaries with parameters sampled on a uniform grid are used. The proposed algorithm exploits the property that damped exponentials can be annihilated by a filter, parameterized by the frequencies and damping factors [20, 106]. This annihilation property implies that a block Toeplitz matrix (convolution matrix) constructed from the signal samples is low-rank [19]. We formulate the recovery of the time domain samples of the signal from its non-uniform samples as a Toeplitz structured low-rank recovery problem. We re-engineer our recent algorithm termed Generic Iteratively Reweighted Annihilating Filter (GIRAF) [88,89] to solve the optimization problem in a reasonable computation time.

In this work [8], we use simulated 2D IR data to demonstrate the qualitative and quantitative performance of the algorithm. The results clearly show the benefit of GIRAF over conventional CS schemes. We observe that non-uniform undersampling provides lower errors than uniform sampling setting for GIRAF, consistent with prior results of CS method. Finally, we apply the method to experimental data of cyanate anion in methanol where the GIRAF algorithm enables nearly exact recovery of experimental data from only 12.5% of the original samples.

4.2 Background

2D IR is a third-order nonlinear spectroscopy technique that uses multiple femtosecond laser pulses to interact with a sample. The response of the sample depends on the timing and geometry of the interactions. We perform our experiments in the pump-probe beam geometry with the first two pulses, produced by pulse shaping,

acting collectively as the pump pulse and the third pulse as the probe. The time delay between pump and probe pulses is denoted by T and is known as the waiting time. The probe also serves as the local oscillator, which we detect by upconverting into the visible and dispersing in a spectrometer for detection in the frequency domain by an array detector. Thus, the response in the ω_3 axis is read off the spectrometer directly on every laser shot, and the coherence time is varied by programming the pulse shaper. A Fourier transform of the interfereogram in τ yields the response in the ω_1 axis. 4.1 gives the 2D spectra where $X_T(\tau, t)$ is the time domain signal at a specific waiting time T.

$$\hat{X}_T(\omega_1, \omega_3) = \sum_{\tau} \sum_{t} \exp\left(-i(\omega_1 \tau + \omega_3 t)\right) X_T(\tau, t) \tag{4.1}$$

In our experiments, 1024 points along ω_3 are read off the array on every laser shot. Around 160-170 different values of τ are collected, followed by apodization and zero-padding to acquire ω_1 to construct a 2D IR spectrum of size 512 x 1024. For a sample with a strong chromophore and high concentration, a single 2D IR spectrum at a given waiting time can be acquired in less than a second, though it is common to average thousands of them to obtain a good signal-to-noise ratio (SNR). For many systems, these acquisitions are repeated several times for each T for signal averaging, and must be collected for various waiting times, leading to experiments lasting for several days. We propose to undersample the τ axis and collect much less than 167 readings and recover the spectra using GIRAF, thus considerably reducing the total number of measurements required and the net measurement time.

4.3 Theory

We will first explain the idea in the 1-D setting, before generalizing to 2-D. Consider the samples of a 1-D damped exponential signal $x(n) = \exp(\beta n S); n = 0, 1, ..N$, where β is the exponential parameter and S is the sampling interval. We note that

if the real part of β is zero, then the signal is an undamped exponential. The key observation is that $x(n)$ is linearly predictable:

$$x(n) = \exp(\beta S)\ x(n-1). \tag{4.2}$$

The above relation can also be expressed as $x * h_\beta = 0$, where $*$ denotes discrete convolution and h_β is a filter with coefficients $[1, -\exp(\beta S)]$. Since the filter kills the signal, $h_\beta[n]$ is termed as the annihilation filter. When the signal is a linear combination of exponentials with parameters $\beta_k; k = 1, .., K$, it still can be annihilated by the filter $h = h_{\beta_1} * h_{\beta_2} * ... h_{\beta_K}$. This annihilation relation can be compactly written as a matrix product

$$\underbrace{\begin{bmatrix} x(K) & x(K-1) & \dots & x(0) \\ \vdots & \vdots & & \\ x(N) & x(N-1) & \dots & x(N-K) \end{bmatrix}}_{\mathcal{T}_K(x)} \underbrace{\begin{bmatrix} h[0] \\ \vdots \\ h[K] \end{bmatrix}}_{\mathbf{h}} = \mathbf{0}, \tag{4.3}$$

where $\mathcal{T}_K(x)$ is the structured convolution matrix. In reality, the number of exponentials in the signal are not known apriori. In this case, one can over-estimate K, when it can be shown that the matrix $\mathcal{T}_K(x)$ is low-rank. This low-rank compactness prior on the structured matrix $\mathcal{T}_K(x)$, which is derived from the signal x, is used to recover the signal from its undersampled measurements [5, 88].

For a specific waiting time, we model the 2D IR signal as the sum of K two dimensional (damped) exponentials:

$$s_T(\tau, t) = \sum_{k=1}^{K} \mathbf{c}_k \underbrace{\exp\left(-\alpha_k \tau - \beta_k t\right)}_{s_k(\tau,t)}, \tag{4.4}$$

sampled on the subset of a uniform grid $[\tau, t]$ of size $M \times N$; $\tau = 0, \lambda, ..(M-1)\lambda; t =$

$0, \eta, ..(N-1)\eta$. Here, $\mathbf{c}_k$ are the weights of the k^{th} exponential, while α_k and β_k are the exponential parameters. Note that this model is equivalent to expressing the spectrum as a linear combination of K Lorentzian functions. As described earlier, smooth spectra such as Voigt profiles can be well-approximated as a linear combination of Lorentzian functions [78].

Similar to the 1-D setting, the $s_k(\tau, t)$ can be annihilated ($s_k * h_k = 0$) by convolution with the filter h_k, where

$$h_k = \begin{bmatrix} 1 & -\exp(\alpha_k \lambda) \\ -\exp(\beta_k \eta) & \exp(\alpha_k \lambda + \beta_k \eta) \end{bmatrix} \tag{4.5}$$

Similar to the 1-D setting, this annihilation relation implies that the block Toeplitz matrix $\mathcal{T}(X_T)$, constructed out of the uniform samples $X_T(\lambda m, \eta n)$ is low-rank. We now use the above low-rank property to recover the unknown entries of X_T, when only a few samples are available:

$$Y^* = \arg\min_Y \operatorname{rank}\left[\mathcal{T}(Y)\right] \quad \text{s.t} \quad Y(\mathbf{s}_l) = X_T(\mathbf{s}_l); l = 1, .., L \tag{4.6}$$

Here, $\mathbf{s}_l; l = 1, .., L$ are the measured samples of X_T. In particular, we search for Y whose samples at $\mathbf{s}_l$ match the measurements and the matrix $\mathcal{T}(Y)$ has the Schatten p norm, which is a convex surrogate for the rank. We relax the combinatorial problem in (4.6) to obtain:

$$Y^* = \arg\min_Y \left(\|\mathcal{T}(Y)\|_p + \frac{\lambda}{2} ||\mathcal{A}(Y) - \mathbf{b}||^2 \right) \tag{4.7}$$

Here, $\mathcal{A}$ is an operator which extracts the samples of Y at the locations $\mathbf{s}_l; l = 1, .., L$ and $\mathbf{b}$ is the length L vector of measured samples. We use the iterative reweighted least squares algorithm [34] to solve the above problem. The final spectrum is obtained by Fourier transformation of the reconstructed Y .

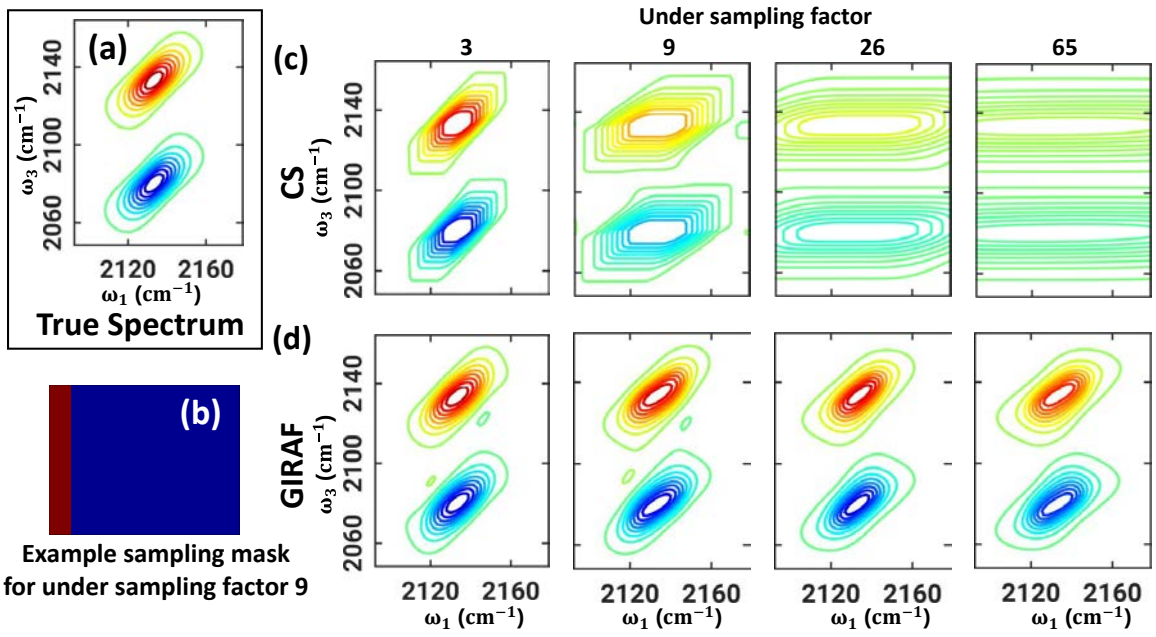

Figure 4.1: Uniformly sampled recovery of simulated data: (a)True 2D spectrum. (b) Example uniform sampling mask for undersampling factor 9; sampled and non-sampled locations are marked in red and blue. (c) Reconstructions using compressed sensing (CS) algorithm and (d) GIRAF at various undersampling factors.

4.4 Experimental Methods

We compare the performance of the proposed method against standard CS methods as in our previous work [53]. We consider both the uniform sampling setting, where data is collected for a few consecutive values of τ, and the algorithm aims to recover it at a higher resolution, and the non-uniform setting where the same number of τ samples are collected but with pseudo-random delays. Previous studies have looked at recovery of exponentials using structured low rank matrices [19, 20, 106] from uniformly sampled data; in this work we compare the performance of GIRAF for uniform and non-uniform sampling. We use two different datasets for our comparison: 1) simulated data using a Kubo lineshape model, 2) experimental 2D IR data for cyanate anion in methanol.

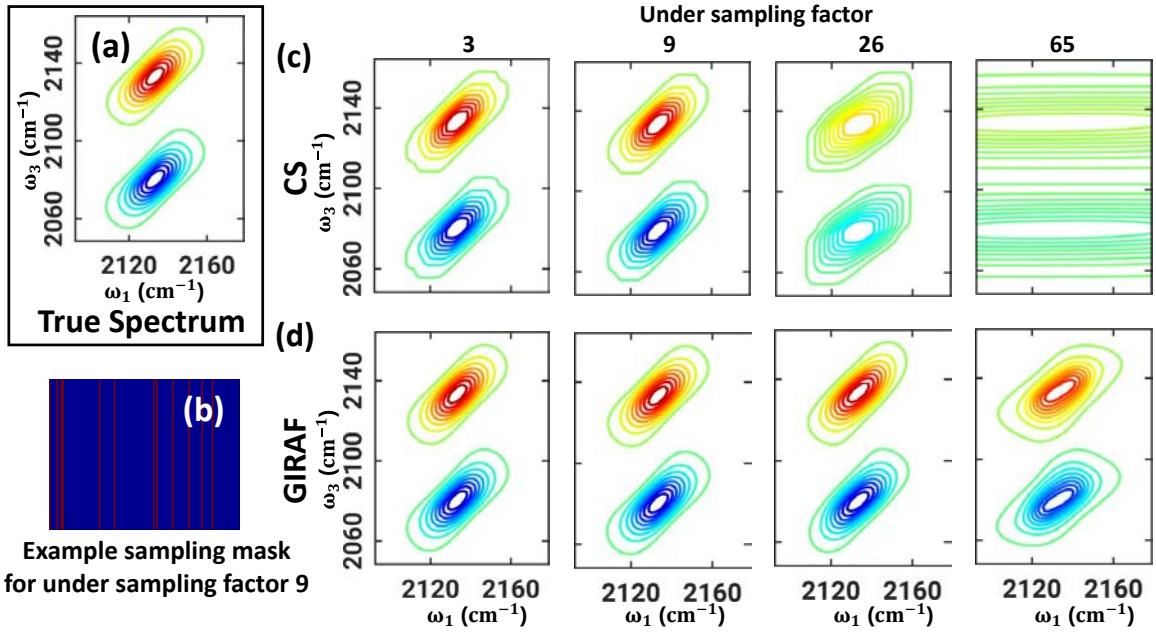

Figure 4.2: Non-uniformly undersampled recovery of simulated data: (a)True 2D spectrum. (b) Example non-uniform sampling mask for undersampling factor 9; sampled and non-sampled locations are marked in red and blue. (c) Reconstructions using compressed sensing (CS) algorithm and (d) GIRAF at various undersampling factors.

4.4.1 Simulated Data

We simulate a purely absorptive 2D spectrum of a 3-level system with a Kubo lineshape model [44], where the fluctuation amplitude is 2 ps^{-1}, the anaharmonicity is 10 ps^{-1}, the correlation time is 1.5 ps and the peak center 10 ps^{-1} is later frequency shifted by 1800 cm^{-1}. The waiting time is chosen to be 0 ps.

We perform uniform and non-uniform undersampled reconstruction of the simulated data and test the robustness of GIRAF in presence of artificially added noise. We added gaussian noise to the time domain data before reconstruction. 3 different noise levels (SNR 20, 25 and 33 dB) are tested. We performed 100 noise realizations at each SNR level and performed fits on them. The results are compared with conventional CS algorithm [53].

A second set of experiments were performed for Kubo lineshape constructed at

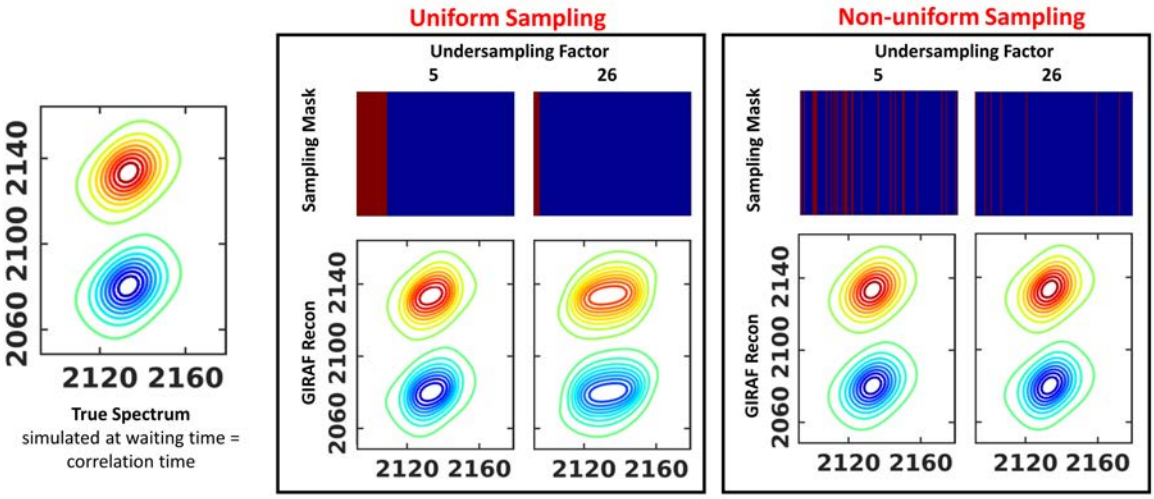

Figure 4.3: Experiment 2 with Kubo-lineshapes: Second set of experiments usinh simulated data of Kubo lineshapes with waiting time equal to correlation time is performed. We observe the same trends for the proposed method.It performs well at very high acceleration factors and also has superior performance for non-uniform undersampling setting.

waiting time equal to correlation time. We evaluate the performance of GIRAF for different lineshapes at different undersampling factors and sampling masks.

4.4.2 Experimental Data

We collected 2D IR data from a sample of 50 mM sodium cyanate in methanol held in a sample cell with a 50 μm path length. The apparatus has been described in detail previously [98], but the most important features are that we have approximately 1 μJ of pump light at the sample and the pump and probe pulses focus to a spot size of approximately 60 μm. At a waiting time of T = 0 ps, we scan τ from 0 4 ps with 24 fs size steps, which is a fully sampled signal because we use phase-increment frequency shifting in our pulse shaper to work in the rotating frame, resulting in 167 τ values. The fully sampled data is then retrospectively, non-uniformly undersampled. We compare the reconstructed experimental data using the proposed method and the conventional CS recovery.

We also extended the algorithm for recovering 2D MR spectroscopic data. A 2-dimensional correlation spectroscopy (COSY) dataset was collected on a Braino phantom at the GE 7T scanner at the University of Iowa. We performed experiments to study the performance of GIRAF for structured and random undersampling upto an undersampling factor of 4.

4.5 Results

4.5.1 Simulated Data Experiments

The reconstructed spectra for the simulated data with uniform and non-uniform sampling patterns are shown in Fig. 4.1 & 4.2, respectively. The true spectrum in Fig. 4.1 & 4.2(a) is obtained by Fourier transforming the fully sampled data. Example masks for undersampling factor 9 are shown in Fig. 4.1 & 4.2(b) for uniform and non-uniform sampling where the sampled locations are marked in red. Reconstruction using CS and GIRAF are shown in the first (c) and second (d) row, respectively. The CS method strives to recover the fewest non-zero spectral intensities resulting in distorted lineshapes at higher undersampling rates, mainly due to the inability of the representation to capture the signal with few data points. GIRAF recovers the line shapes with high fidelity. Both methods perform better in the non-uniform sampling case as is expected, because the coherent undersampling artifacts from uniform sampling are greater than the incoherent artifacts from pseudo-random undersampling. We fit the results to a 2D Gaussian lineshape for quantitative comparison (fitting model explained in ref [53]). Fig.4.4 demonstrates the ability of GIRAF and CS to recover lineshape details at different undersampling factors and SNR levels. We experimented on 100 noise realizations for every undersampling factor and SNR level and have reported the mean and standard deviation of the line fit parameters. Peak amplitudes are suppressed with increasing undersampling, which is much worse for CS. The center and width of peaks are reported only for the dimension that is undersampled. GIRAF outperforms CS according to fit results. Even in presence of noise

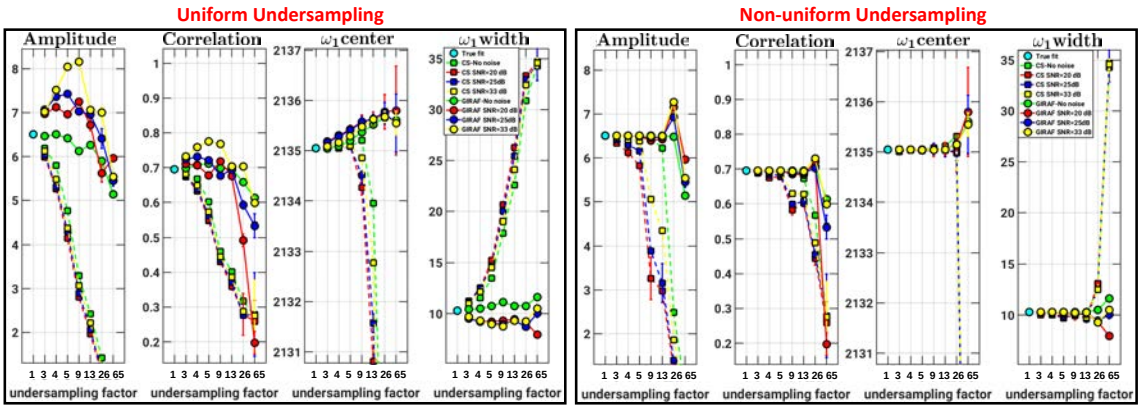

Figure 4.4: Simulated Data 2D Gaussian fits at different noise levels: Mean and standard deviation of the fit parameters for uniform and non-uniform undersampling are shown. 100 experiments per noise realization were performed. CS parameters degrade rapidly with increasing acceleration whereas the degradation of GIRAF fits is remarkably less. Note that the non-uniform setting performs better than uniform setting.

we observe the performance of GIRAF is highly reliable especially for non-uniform undersampling. The correlation parameter, in case of GIRAF, slightly increases before decreasing at higher undersampling for uniform setting and shows more stable behavior in the nonuniform setting, in contrast to CS where it monotonically decreases. Thus it can be concluded that the proposed method is robust in presence of noise. It quantitatively recovers lineshapes up to undersampling factor of 26 *i.e.* only 3.8% of the samples. Even at undersampling factor of 65, *i.e.* only 2 τ lines, the GIRAF reconstruction results in only a 15% error in the correlation parameter.

Also in the second set of experiments as shown in Fig. 4.3 we observe optimal performance of GIRAF for undersampling factors 5 and 26. We compared the performance for uniform and non-uniform sampling masks. Similar trends were observed. GIRAF performed well in retaining lineshapes even at high acceleration factors and was better with non-uniform undersampling.

4.5.2 Real Data Experiments

Due to the superior performance of non-uniform sampling, we restrict our analysis to this setting for the experimental data. The true spectrum is shown in Fig. 4.5(a) and an example sampling mask for factor 10, with sampled locations in red, is shown in (b). Similar to the simulated case, the performance of CS method (c) is compromised at high compression factors. GIRAF (d) recovers the lineshapes with almost no distortion up to an undersampling factor of 8, *i.e.* only 12.5% of the fully sampled measurements, thus performing reasonably even at higher undersampling.

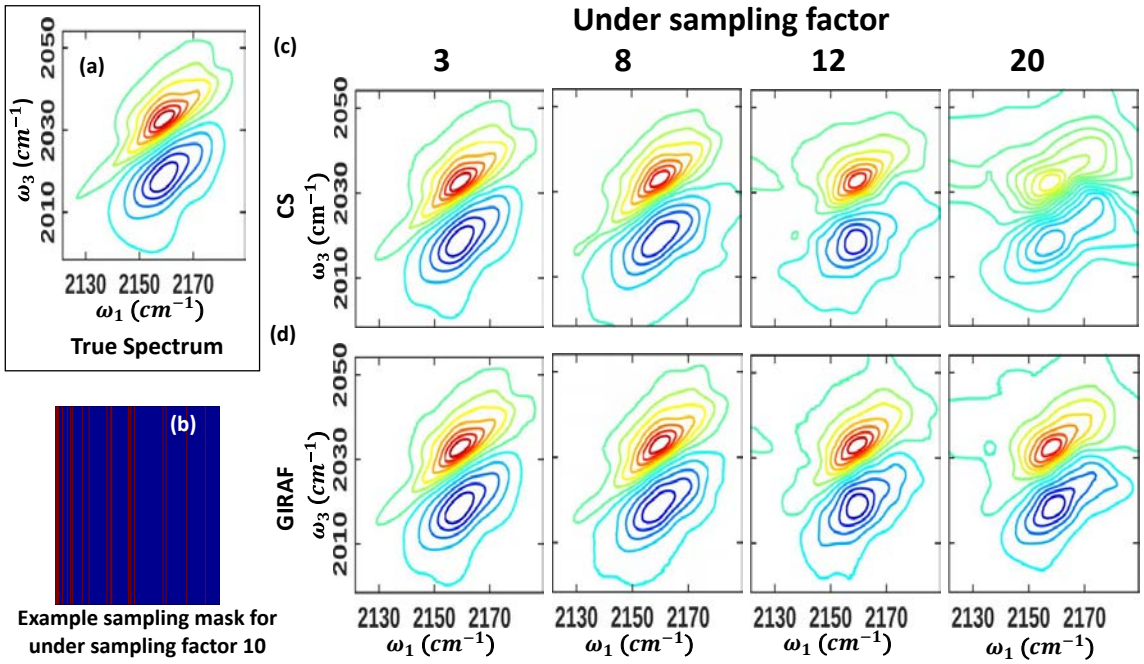

Figure 4.5: Non-uniformly undersampled recovery of experimental 2D IR data: (a)The fully sampled 2D spectrum is recovered from 167 τ points. (b) Example non-uniform sampling mask of undersampling factor 10 where sampled locations are marked in red and non-sampled locations in blue. (c) Performance of compressed sensing (CS) algorithm and (d) GIRAF at various undersampling factors.

Fig.4.6 shows a quantitative comparison of 2D Gaussian fit parameters. GIRAF

lineshape parameters deviate ±10% of the true data upto undersampling factor of 20. CS fits, however, significantly deviate from the true fits beyond undersampling factor of 5. For experimental data, which has more complicated lineshape than simulated data, GIRAF exhibits superior recovery.

Fig.4.7 shows the qualitative performance of the proposed method for both uniform/windowed and non-uniform undersampling. The experiments are performed at an acceleration factor of 4 or in other words the data is recovered from only 25 % of samples. It is observed that though both sampling schemes have remarkable recovery the non-uniform sampling scheme is able to preserve the lineshapes.

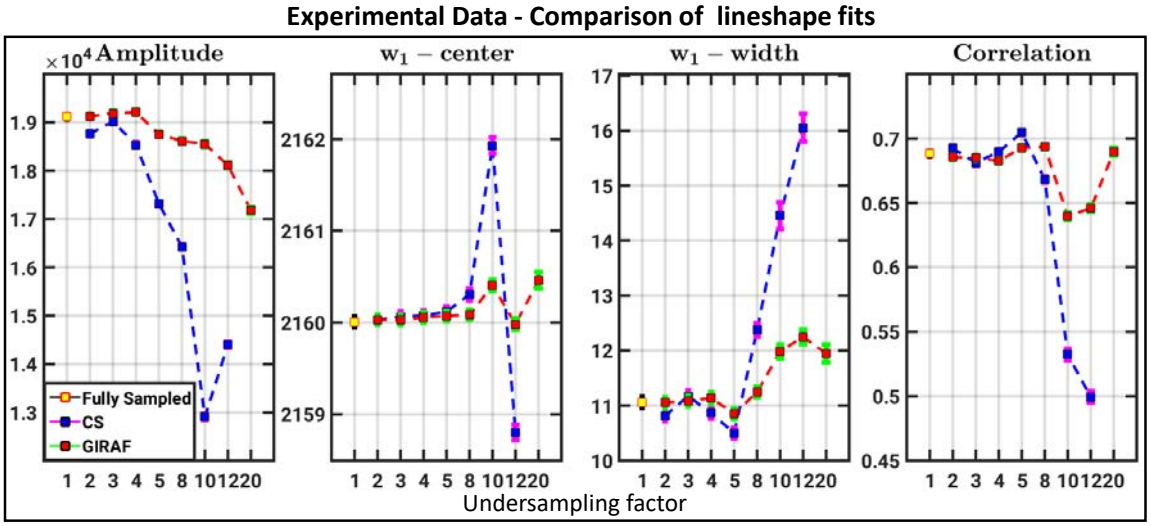

Figure 4.6: Gaussian fit comparisons for experimental data: Fit parameters for CS and GIRAF reconstructions are shown. Error bars represent 95% confidence bounds. CS reconstruction for undersampling factor 20 are not reported in the plot because it could not be fitted to the model due to severe distortion of the lineshape. Lineshape fits for CS reconstruction degrade rapidly with increasing acceleration factor whereas the GIRAF results are within ± 10% of the true fits.

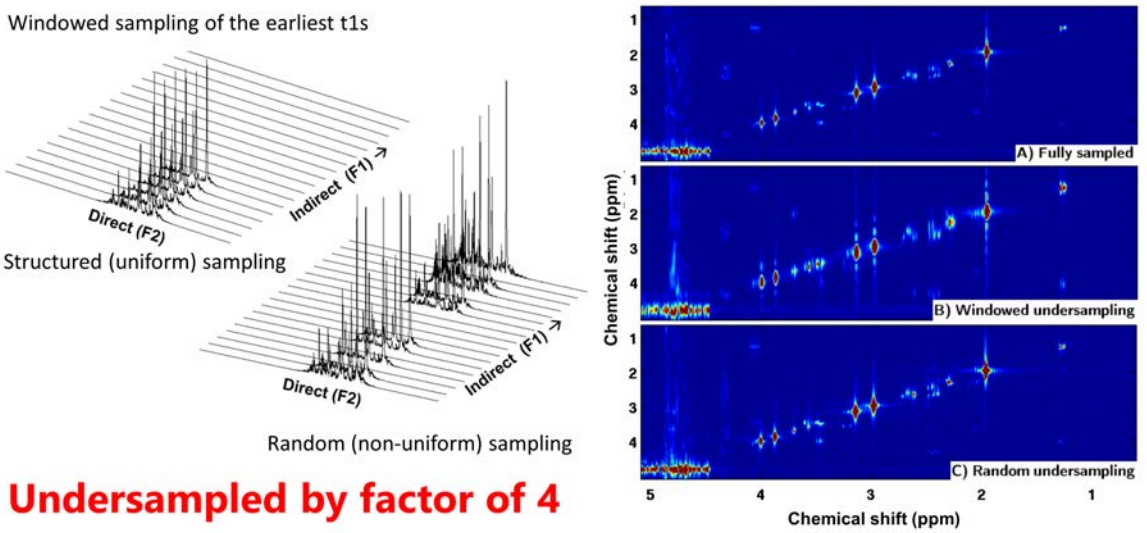

Figure 4.7: 2D COSY 7T MR experiments: Data collected from a 7T MR scanner was used to evaluate GIRAF. Data from 2D COSY experiments were undersampled by a factor of 4 for both non-uniform and uniform/windowed setting. The reconstruction for non-uniform sampling preserves all peaks and shapes.

4.6 Conclusion

In summary, we introduced a novel method to reconstruct 2D IR data from few measurements. The proposed algorithm models the signal as a linear combination of damped exponentials. The algorithm exploits the low rank structure of a Toeplitz matrix, whose entries are samples of the linear combination of exponentials, and is capable of recovering the missing signal samples from heavily undersampled measurements. Our results show that the lineshapes are adequately preserved for quantitative analysis, with as few as 3.8% & 8% samples for the simulated and experimental data respectively. This work introduces a very promising method with the potential to accelerate 2D IR considerably. Detailed analyses of the method and its range of applications are crucial, however, and are the subject of further ongoing studies.

CHAPTER 5
CONCLUSIONS & FUTURE DIRECTIONS

5.1 Conclusions

In this PhD work, we have proposed several novel reconstruction methods for advancement of MRSI. The major limitations of spectroscopic imaging are attended and signal models and data driven priors are exploited to solve these limitations. Firstly we attempt to surmount the intrinsic limitations of MRSI by using a low-rank framework for recovery of investigated data. Following that we also introduce a novel algorithm to remove spectral artifacts in high resolution MRSI which appears to be a bottleneck in using EPSI for increased resolution acquisition especially at higher field strengths. Finally we also develop a structured low rank recovery algorithm for accelerating 2D IR and MR data. In the following sections, we revisit our primary findings and contributions and discuss further research directions.

In chapter 2 we introduce a novel compartmentalized low-rank algorithm with orthogonality constraint which enables reconstruction of high resolution metabolite maps without the use of any lipid suppression methods. The proposed method is effective at short TE (55 ms) acquisitions also. Also an efficient dual-density data acquisition method using variable density spirals has been introduced to achieve high resolution lipid estimates in a feasible scan time. We demonstrated in this work with simulate and real experiments that high resolution maps can be recovered using the low-rank models and orthogonality priors. Similar performance for both lipid suppressed and unsuppressed data was observed, thus signifying this method to be applicable for all datasets including challenging ones with lipid leakage. Removing lipid artifacts using reconstruction techniques serves as a great alternative for existing methods which result in reduced volume coverage or further decrease of metabolite signal.

In chapter 3 we proposed a novel algorithm for denoising and deinterleaving of

EPSI data without directly estimating phase or relying on theoretical k-space trajectory. We further demonstrated the improvement offered by the proposed method compared to the classical phase correction method. The proposed scheme would be highly beneficial in reconstruction and correction of high-resolution EPSI, especially for the acquisition from high field magnets. We demonstrated the performance across different datasets. Specifically ^{13}C mouse kidney MRSI data collected using bipolar gradients at 9.4 T was used to study the performance of the proposed method at high field magnets. We further validated the performance on more noisy and challenging datasets. Two sets of ^{1}H *in-vivo* MRSI data was used for this purpose. We can appreciate the effect of denoising provided by the different low rank priors through these experiments.

In chapter 4 we introduced a novel method to reconstruct 2D IR data from few measurements. The proposed algorithm models the signal as a linear combination of damped exponentials. The algorithm exploits the low rank structure of a Toeplitz matrix, whose entries are samples of the linear combination of exponentials, and is capable of recovering the missing signal samples from heavily undersampled measurements. Our results show that the lineshapes are adequately preserved for quantitative analysis, with as few as 3.8% & 8% samples for the simulated and experimental data respectively. This work introduces a very promising method with the potential to accelerate 2D IR considerably. We also demonstrate the performance of this method on 2D MR spectroscopic data. Detailed analyses of the method and its range of applications are crucial, however, and are the subject of further ongoing studies.

5.2 Future Directions

The reconstruction techniques developed in this thesis are ultimately targeted towards clinical utility. Moreover the work tackles with several individual pieces in the several technical challenges in MRSI. To fully evaluate the efficiency and reproducibility of the developed methods in the clinical routine, a systematic study on a large

number of patient scans is needed. Also several new methods can be proposed by combining priors explores in this thesis to come develop comprehensive MRSI studies.

n this section, we list a few potential methods combining ideas proposed, and also list potential directions in terms of clinically validating the methods.

- **Extension to 4-D spectroscopy:** 3D acquisitions have advantages over multislice 2D imaging in terms of providing contiguous spatial coverage. For full brain coverage , 3D spatial and 1D spectroscopic data needs to be reconstructed at a feasible scan time. However lipid leakage artifacts are worse as it is cumbersome to suppress all the lipids when collecting whole brain data. Algorithms using priors from compartmentalized low-rank models and lipid basis orthogonality can help achieve full brain exams in a feasible scan time without much set-up time for lipid suppression bands.

- **Extension to 5-D spectroscopy:** Multi-dimensional spectroscopy reveals richer metabolic information by improved resolution of overlapping spectra. However with 2 added dimensions the experimental time increases. Combining different low-rank priors we can achieve acceleration and denoising of experimental data.

- **Extension to 3-D experiments for IR spectroscopy:** 2D IR spectroscopy is a tool we use to study transient molecular structure and dynamics in solution. As a vibrational spectroscopy, it directly interrogates the vibrations of chemical bonds and how the vibrations interact with one another.However to understand the dynamics needs ro be studied over time which adds a third dimension. We could extend the GIRAF algorithm to 3D setting where we estimate 3D annihilation filters to accelerate experiments.

- **Evaluation on large clinical datasets:** Finally all these methods would only achieve fruition on being evaluated on a clinical setting. A very important

future direction would be testing these on patient groups, for example multiple sclerosis (MS) or brain tumor groups to see if it can reveal metabolite maps similar to existing methods at a higher resolution and accuracy.

REFERENCES

[1] E. Adalsteinsson, E. Sullivan, N. Kleinhans, D. Spielman, and A. Pfefferbaum, "Longitudinal decline of the neuronal marker n-acetyl aspartate in alzheimer's disease," *The Lancet*, vol. 355, no. 9216, pp. 1696–1697, 2000.

[2] E. Adalsteinsson, J. Star-Lack, C. H. Meyer, and D. M. Spielman, "Reduced spatial side lobes in chemical-shift imaging," *Magn Reson Med*, vol. 42, no. 2, pp. 314–323, 1999.

[3] J. Almeida, J. Prior, and M. Plenio, "Computation of 2-d spectra assisted by compressed sampling," *arXiv preprint arXiv:1207.2404*, 2012.

[4] S. Antel, L. Li, F. Cendes, D. Collins, R. Kearney, R. Shinghal, and D. Arnold, "Predicting surgical outcome in temporal lobe epilepsy patients using mri and mrsi," *Neurology*, vol. 58, no. 10, pp. 1505–1512, 2002.

[5] A. Balachandrasekaran, V. Magnotta, and M. Jacob, "Recovery of damped exponentials using structured low rank matrix completion," *arXiv preprint arXiv:1704.04511*, 2017.

[6] Y. Bao and A. A. Maudsley, "Improved reconstruction for MR spectroscopic imaging," *IEEE Trans Med Imaging*, vol. 26, no. 5, pp. 686–695, 2007.

[7] H. Barkhuijsen, R. De Beer, and D. Van Ormondt, "Improved algorithm for noniterative time-domain model fitting to exponentially damped magnetic resonance signals," *J Magn Reson*, vol. 73, no. 3, pp. 553–557, 1987.

[8] I. Bhattacharya, J. J. Humston, C. M. Cheatum, and M. Jacob, "Accelerating two-dimensional infrared spectroscopy while preserving lineshapes using giraf," *Optics letters*, vol. 42, no. 22, pp. 4573–4576, 2017.

[9] I. Bhattacharya and M. Jacob, "Compartmentalized low-rank regularization with orthogonality constraints for high-resolution mrsi," in *ISBI*. IEEE, 2016, pp. 960–963.

[10] I. Bhattacharya and M. Jacob, "Compartmentalized low-rank recovery for high-resolution lipid unsuppressed mrsi," *MRM*, vol. 78, no. 4, pp. 1267–1280, 2017.

[11] S. Bhave, R. Eslami, and M. Jacob, "Sparse spectral deconvolution algorithm for noncartesian MR spectroscopic imaging." *Magn Reson Med*, vol. 71, no. 2, pp. 469–76, 2014.

[12] S. Bhave, R. Eslami, and M. Jacob, "Sparse spectral deconvolution algorithm for noncartesian mr spectroscopic imaging," *Magnetic resonance in medicine*, vol. 71, no. 2, pp. 469–476, 2014.

[13] B. Bilgic, B. Gagoski, T. Kok, and E. Adalsteinsson, "Lipid suppression in csi with spatial priors and highly undersampled peripheral k-space," *Magn Reson Med*, vol. 69, no. 6, pp. 1501–1511, 2013.

[14] P. A. Bottomley, "Spatial Localization in NMR Spectroscopy in Vivo," *Ann NY Acad Sci*, vol. 508, no. 1 Physiological, pp. 333–348, 1987.

[15] T. Brown, B. Kincaid, and K. Ugurbil, "NMR chemical shift imaging in three dimensions," *Proc Natl Acad Sci USA*, vol. 79, no. 11, pp. 3523–3526, 1982.

[16] G. Bydder and I. Young, "MR imaging: clinical use of the inversion recovery sequence." *J Comput Assist Tomogr*, vol. 9, no. 4, pp. 659–675, 1985.

[17] E. Candes, C. Sing-Long, J. D. Trzasko, *et al.*, "Unbiased risk estimates for singular value thresholding and spectral estimators," *IEEE Trans Med Imaging*, vol. 61, no. 19, pp. 4643–4657, 2013.

[18] A. A. Chan, A. Lau, A. Pirzkall, S. M. Chang, L. J. Verhey, D. Larson, M. W. McDermott, W. P. Dillon, and S. J. Nelson, "Proton magnetic resonance spectroscopy imaging in the evaluation of patients undergoing gamma knife surgery for grade iv glioma," 2004.

[19] Y. Chen and Y. Chi, "Robust spectral compressed sensing via structured matrix completion," in *IEEE Trans. Inf. Theory*, vol. 60, no. 10, 2014, pp. 6576–6601.

[20] Q. Cheng and H. Yingbo, *A review of parametric high-resolution methods,High-resolution and robust signal processing (H. Yingbo, A. Gershman, and Q. Cheng, eds.),*. Marcel Dekker, 2003.

[21] A. Chu, J. R. Alger, G. J. Moore, and S. Posse, "Proton echo-planar spectroscopic imaging with highly effective outer volume suppression using combined presaturation and spatially selective echo dephasing." *Magn Reson Med*, vol. 49, no. 5, pp. 817–21, 2003.

[22] C. Cui, X. Wu, J. D. Newell, and M. Jacob, "Fat water decomposition using globally optimal surface estimation (GOOSE) algorithm." *Magn Reson Med*, vol. 73, no. 3, pp. 1289–1299, 2015.

[23] S. R. Dager, N. Oskin, T. L. Richards, and S. Posse, "Research applications of magnetic resonance spectroscopy (mrs) to investigate psychiatric disorders," *Topics in magnetic resonance imaging: TMRI*, vol. 19, no. 2, p. 81, 2008.

[24] R. A. De Graaf, *In vivo NMR spectroscopy: principles and techniques*. John Wiley & Sons, 2013.

[25] R. A. de Graaf and K. Nicolay, "Adiabatic water suppression using frequency selective excitation," *Magn Reson Med*, vol. 40, no. 5, pp. 690–696, 1998.

[26] W. Du, Y. P. Du, X. Fan, M. A. Zamora, and G. S. Karczmar, "Reduction of spectral ghost artifacts in high-resolution echo-planar spectroscopic imaging of water and fat resonances," *MRM*, vol. 49, no. 6, pp. 1113–1120, 2003.

[27] J. A. Dunbar, D. G. Osborne, J. M. Anna, and K. J. Kubarych, "Accelerated 2D-IR using compressed sensing," *The Journal of Physical Chemistry Letters*, vol. 4, no. 15, pp. 2489–2492, 2013.

[28] J. H. Duyn, J. Gillen, G. Sobering, P. C. Van Zijl, and C. T. Moonen, "Multisection proton mr spectroscopic imaging of the brain." *Radiology*, vol. 188, no. 1, pp. 277–282, 1993.

[29] A. Ebel, V. Govindaraju, and A. A. Maudsley, "Comparison of inversion recovery preparation schemes for lipid suppression in ^{1}H MRSI of human brain." *Magn Reson Med*, vol. 49, no. 5, pp. 903–908, 2003.

[30] A. Ebel and A. A. Maudsley, "Comparison of methods for reduction of lipid contamination for in vivo proton MR spectroscopic imaging of the brain," *Magn Reson Med*, vol. 46, no. 4, pp. 706–712, 2001.

[31] A. Ebel, B. J. Soher, and A. A. Maudsley, "Assessment of 3d proton mr echo-planar spectroscopic imaging using automated spectral analysis," *MRM*, vol. 46, no. 6, pp. 1072–1078, 2001.

[32] R. Eslami and M. Jacob, "Robust reconstruction of MRSI data using a sparse spectral model and high resolution MRI priors." *IEEE Trans Med Imaging*, vol. 29, no. 6, pp. 1297–309, 2010.

[33] R. Eslami and M. Jacob, "Robust reconstruction of mrsi data using a sparse spectral model and high resolution mri priors," *IEEE transactions on medical imaging*, vol. 29, no. 6, pp. 1297–1309, 2010.

[34] M. Fornasier, H. Rauhut, and R. Ward, "Low-rank matrix recovery via iteratively reweighted least squares minimization," *SIAM J Optimization*, vol. 21, no. 4, pp. 1614–1640, 2011.

[35] T. Fujimoto, T. Nakano, T. Takano, Y. Hokazono, T. Asakura, and T. Tsuji, "Study of chronic schizophrenics using 31p magnetic resonance chemical shift imaging," *Acta Psychiatrica Scandinavica*, vol. 86, no. 6, pp. 455–462, 1992.

[36] W. A. Gomes, F. A. Lado, N. C. de Lanerolle, K. Takahashi, C. Pan, and H. P. Hetherington, "Spectroscopic imaging of the pilocarpine model of human epilepsy suggests that early NAA reduction predicts epilepsy." *Magn Reson Med*, vol. 58, no. 2, pp. 230–5, 2007.

[37] O. Gonen, T. A. Oberndorfer, M. Inglese, J. S. Babb, J. Herbert, and R. I. Grossman, "Reproducibility of three whole-brain N-acetylaspartate decline cohorts in relapsing-remitting multiple sclerosis," *Am J Neuroradiol*, vol. 28, no. 2, pp. 267–271, 2007.

[38] V. Govindaraju, K. Young, and A. A. Maudsley, "Proton NMR chemical shifts and coupling constants for brain metabolites," *NMR Biomed*, vol. 13, no. 3, pp. 129–153, 2000.

[39] E. E. Graves, S. J. Nelson, D. B. Vigneron, C. Chin, L. Verhey, M. McDermott, D. Larson, P. K. Sneed, S. Chang, M. D. Prados, *et al.*, "A preliminary study of the prognostic value of proton magnetic resonance spectroscopic imaging in gamma knife radiosurgery of recurrent malignant gliomas," *Neurosurgery*, vol. 46, no. 2, pp. 319–319, 2000.

[40] M. Guerquin-Kern, L. Lejeune, K. P. Pruessmann, and M. Unser, "Realistic analytical phantoms for parallel magnetic resonance imaging," *IEEE Trans Med Imaging*, vol. 31, no. 3, pp. 626–636, 2012.

[41] A. Haase, J. Frahm, W. Hanicke, and D. Matthaei, "^{1}H NMR chemical shift selective (CHESS) imaging," *Phys Med Biol*, vol. 30, no. 4, p. 341, 1985.

[42] J. P. Haldar and Z.-P. Liang, "Spatiotemporal imaging with partially separable functions: a matrix recovery approach," in *IEEE International Symposium on Biomedical Imaging: From Nano to Macro, 2010. ISBI 2010, IEEE*, 2010, pp. 716–719.

[43] P. Hamm, M. Lim, and R. M. Hochstrasser, "Structure of the amide i band of peptides measured by femtosecond nonlinear-infrared spectroscopy," *The Journal of Physical Chemistry B*, vol. 102, no. 31, pp. 6123–6138, 1998.

[44] P. Hamm and M. Zanni, *Concepts and methods of 2D infrared spectroscopy*. Cambridge University Press, 2011.

[45] L. G. Hanson, K. Schaumburg, and O. B. Paulson, "Reconstruction strategy for echo planar spectroscopy and its application to partially undersampled imaging," *MRM*, vol. 44, no. 3, pp. 412–417, 2000.

[46] C. I. Haupt, N. Schuff, M. W. Weiner, and A. A. Maudsley, "Removal of lipid artifacts in ^{1}H spectroscopic imaging by data extrapolation," *Magn Reson Med*, vol. 35, no. 5, pp. 678–687, 1996.

[47] A. Horská and P. B. Barker, "Imaging of brain tumors: Mr spectroscopy and metabolic imaging," *Neuroimaging clinics of North America*, vol. 20, no. 3, pp. 293–310, 2010.

[48] R. Hourani, L. Brant, T. Rizk, J. Weingart, P. Barker, and A. Horska, "Can proton mr spectroscopic and perfusion imaging differentiate between neoplastic and nonneoplastic brain lesions in adults?" *American Journal of Neuroradiology*, vol. 29, no. 2, pp. 366–372, 2008.

[49] X. P. Hu, M. Patel, W. Chen, and K. Ugurbil, "Reduction of truncation artifacts in chemical-shift imaging by extended sampling using variable repetition time," *J Magn Reson Series B*, vol. 106, no. 3, pp. 292–296, 1995.

[50] X. P. Hu, M. Patel, and K. Ugurbil, "A new strategy for spectroscopic imaging," *J Magn Reson Series B*, vol. 103, no. 1, pp. 30–38, 1994.

[51] X. Hu, D. N. Levin, P. C. Lauterbur, and T. Spraggins, "SLIM: Spectral localization by imaging," *Magn Reson Med*, vol. 8, no. 3, pp. 314–322, 1988.

[52] X. Hu and A. E. Stillman, "Technique for reduction of truncation artifact in chemical shift images," *IEEE Trans Med Imaging*, vol. 10, no. 3, pp. 290–294, 1991.

[53] J. J. Humston, I. Bhattacharya, M. Jacob, and C. M. Cheatum, "Compressively sampled two-dimensional infrared spectroscopy that preserves line shape information," *The Journal of Physical Chemistry A*, vol. 121, no. 16, pp. 3088–3093, 2017.

[54] M. Jacob, X. Zhu, A. Ebel, N. Schuff, and Z.-P. Liang, "Improved model-based magnetic resonance spectroscopic imaging," *IEEE Trans Med Imaging*, vol. 26, no. 10, pp. 1305–1318, 2007.

[55] M. A. Jacobs, P. B. Barker, P. A. Bottomley, Z. Bhujwalla, and D. A. Bluemke, "Proton magnetic resonance spectroscopic imaging of human breast cancer: a preliminary study," *Journal of Magnetic Resonance Imaging*, vol. 19, no. 1, pp. 68–75, 2004.

[56] J. Kasten, A. Klauser, F. Lazeyras, and D. Van De Ville, "Magnetic Resonance Spectroscopic Imaging at Superresolution: Overview and Perspectives," *J Magn Reson*, 2015.

[57] J. Kasten, F. Lazeyras, and D. Van De Ville, "Data-driven MRSI spectral localization using non-cartesian sampling trajectories," in *IEEE 10th International Symposium on Biomedical Imaging (ISBI) ,2013*, 2013, pp. 958–961.

[58] J. Kasten, F. Lazeyras, and D. Van De Ville, "Data-driven MRSI spectral localization via low-rank component analysis." *IEEE Trans Med Imaging*, vol. 32, no. 10, pp. 1853–1863, 2013.

[59] J. A. Kasten, "Superresolution Reconstruction for Magnetic Resonance Spectroscopic Imaging Exploiting Low-Rank Spatio-Spectral Structure," Ph.D. dissertation, EPFL, 2015.

[60] I. Khalidov, D. Van De Ville, M. Jacob, F. Lazeyras, and M. Unser, "BSLIM: Spectral localization by imaging with explicit field inhomogeneity compensation," *IEEE Trans Med Imaging*, vol. 26, no. 7, pp. 990–1000, 2007.

[61] J. Knight-Scott, "Application of multiple inversion recovery for suppression of macromolecule resonances in short echo time ^{1}H NMR spectroscopy of human brain." *J Magn Reson*, vol. 140, no. 1, pp. 228–234, 1999.

[62] J. Kurhanewicz, M. G. Swanson, S. J. Nelson, and D. B. Vigneron, "Combined magnetic resonance imaging and spectroscopic imaging approach to molecular imaging of prostate cancer," *Journal of Magnetic Resonance Imaging*, vol. 16, no. 4, pp. 451–463, 2002.

[63] F. Lam and Z. P. Liang, "A subspace approach to high-resolution spectroscopic imaging." *Magn Reson Med*, vol. 71, no. 4, pp. 1349–1357, 2014.

[64] F. Lam, C. Ma, B. Clifford, C. L. Johnson, and Z.-P. Liang, "High-resolution ^{1}H-MRSI of the brain using SPICE: Data acquisition and image reconstruction," *Magn Reson Med*, 2015.

[65] P. Le Roux, R. J. Gilles, G. C. McKinnon, and P. G. Carlier, "Optimized outer volume suppression for single-shot fast spin-echo cardiac imaging," *J Magn Reson Imaging*, vol. 8, no. 5, pp. 1022–1032, 1998.

[66] J. Lee, K. H. Jin, and J. C. Ye, "Reference-free single-pass epi nyquist ghost correction using annihilating filter-based low rank hankel matrix (aloha)," *MRM*, vol. 76, no. 6, pp. 1775–1789, 2016.

[67] L. Li, F. Cendes, S. Antel, F. Andermann, W. Serles, F. Dubeau, A. Olivier, and D. Arnold, "Prognostic value of proton magnetic resonance spectroscopic imaging for surgical outcome in patients with intractable temporal lobe epilepsy and bilateral hippocampal atrophy," *Annals of neurology*, vol. 47, no. 2, pp. 195–200, 2000.

[68] D. Liang, B. Liu, J. Wang, and L. Ying, "Accelerating SENSE using compressed sensing," *Magn Reson Med*, vol. 62, no. 6, pp. 1574–1584, 2009.

[69] Z.-P. Liang and P. C. Lauterbur, "A generalized series approach to MR spectroscopic imaging," *IEEE Trans Med Imaging*, vol. 10, no. 2, pp. 132–137, 1991.

[70] S. G. Lingala, Y. Hu, E. DiBella, and M. Jacob, "Accelerated dynamic MRI exploiting sparsity and low-rank structure: kt SLR," *IEEE Trans Med Imaging*, vol. 30, no. 5, pp. 1042–1054, 2011.

[71] S. G. Lingala and M. Jacob, "Blind compressive sensing dynamic MRI," *IEEE Trans Med Imaging*, vol. 32, no. 6, p. 1132, 2013.

[72] Y. Liu, C. Ma, B. Clifford, F. Lam, C. Johnson, and Z.-P. Liang, "Improved low-rank filtering of magnetic resonance spectroscopic imaging data corrupted by noise and B0 field inhomogeneity," *IEEE Trans Biomed Eng*, 2015.

[73] R. A. Lobos, T. H. Kim, W. S. Hoge, and J. P. Haldar, "Navigator-free epi ghost correction using low-rank matrix modeling: Theoretical insights and practical improvements," in *Proc. ISMRM*, 2017, p. 0449.

[74] Y. Luo, R. A. Graaf, L. Delabarre, A. Tannus, and M. Garwood, "BISTRO : An outer-volume suppression method that tolerates RF field inhomogeneity," *Magn Reson Med*, vol. 45, no. 6, pp. 1095–1102, 2001.

[75] C. Ma, F. Lam, C. L. Johnson, and Z.-P. Liang, "Removal of nuisance signals from limited and sparse ^{1}H MRSI data using a union-of-subspaces model," *Magn Reson Med*, Mar 2015.

[76] M. Mani, M. Jacob, D. Kelley, and V. Magnotta, "Multi-shot sensitivity-encoded diffusion data recovery using structured low-rank matrix completion (mussels)," *MRM*, vol. 78, no. 2, pp. 494–507, 2017.

[77] A. J. Martin, H. Liu, W. A. Hall, and C. L. Truwit, "Preliminary assessment of turbo spectroscopic imaging for targeting in brain biopsy," *American journal of neuroradiology*, vol. 22, no. 5, pp. 959–968, 2001.

[78] P. Martin and J. Puerta, "Generalized lorentzian approximations for the voigt line shape," *Applied optics*, vol. 20, no. 2, pp. 259–263, 1981.

[79] A. A. Maudsley, C. Domenig, V. Govind, A. Darkazanli, C. Studholme, K. Arheart, and C. Bloomer, "Mapping of brain metabolite distributions by volumetric proton MR spectroscopic imaging (MRSI)," *Magn Reson Med*, vol. 61, no. 3, pp. 548–559, 2009.

[80] T. R. McKnight, K. R. Lamborn, T. D. Love, M. S. Berger, S. Chang, W. P. Dillon, A. Bollen, and S. J. Nelson, "Correlation of magnetic resonance spectroscopic and growth characteristics within Grades II and III gliomas," *J Neurosurg*, vol. 106, no. 4, pp. 660–666, 2007.

[81] G. Metzger and X. Hu, "Application of interlaced fourier transform to echo-planar spectroscopic imaging," *JMR*, vol. 125, no. 1, pp. 166–170, 1997.

[82] G. Metzger, S. Sarkar, X. Zhang, K. Heberlein, M. Patel, and X. Hu, "A hybrid technique for spectroscopic imaging with reduced truncation artifact," *Magn Reson Imaging*, vol. 17, no. 3, pp. 435–443, 1999.

[83] K. Mohan and M. Fazel, "Iterative reweighted algorithms for matrix rank minimization," *Journal of Machine Learning Research*, vol. 13, no. 1, pp. 3441–3473, 2012.

[84] S. J. Nelson, "Multivoxel magnetic resonance spectroscopy of brain tumors1," *Molecular Cancer Therapeutics*, vol. 2, no. 5, pp. 497–507, 2003.

[85] H. M. Nguyen, X. Peng, M. N. Do, and Z. P. Liang, "Denoising MR spectroscopic imaging data with low-rank approximations," *IEEE Trans Biomed Eng*, vol. 60, no. 1, pp. 78–89, 2013.

[86] R. J. Ogg, R. B. Kingsley, and J. S. Taylor, "WET, a T_1-and B_1-insensitive water-suppression method for in vivo localized 1 H NMR spectroscopy," *J Magn Reson B*, vol. 104, no. 1, pp. 1–10, 1994.

[87] A. M. Omuro, C. C. Leite, K. Mokhtari, and J.-Y. Delattre, "Pitfalls in the diagnosis of brain tumours," *The Lancet Neurology*, vol. 5, no. 11, pp. 937–948, 2006.

[88] G. Ongie and M. Jacob, "Recovery of piecewise smooth images from few fourier samples," in *Sampling Theory and Applications (SampTA), 2015 International Conference on*. IEEE, 2015, pp. 543–547.

[89] G. Ongie and M. Jacob, "A fast algorithm for convolutional structured low-rank matrix recovery," *IEEE Transactions on Computational Imaging*, 2017.

[90] G. Payne and M. Leach, "Applications of magnetic resonance spectroscopy in radiotherapy treatment planning," *The British journal of radiology*, vol. 79, no. special_issue_1, pp. S16–S26, 2006.

[91] X. Peng, H. Nguyen, J. Haldar, D. Hernando, X. P. Wang, and Z. P. Liang, "Correction of field inhomogeneity effects on limited k-space MRSI data using anatomical constraints," in *Conf Proc IEEE Eng Med Biol Soc (EMBC)*, 2010, pp. 883–886.

[92] J. G. Pipe and N. R. Zwart, "Spiral trajectory design: a flexible numerical algorithm and base analytical equations." *Magn Reson Med*, vol. 71, no. 1, pp. 278–285, 2014.

[93] A. Pirzkall, T. R. McKnight, E. E. Graves, M. P. Carol, P. K. Sneed, W. W. Wara, S. J. Nelson, L. J. Verhey, and D. A. Larson, "Mr-spectroscopy guided target delineation for high-grade gliomas," *International Journal of Radiation Oncology* Biology* Physics*, vol. 50, no. 4, pp. 915–928, 2001.

[94] S. K. Plevritis and A. Macovski, "MRS imaging using anatomically based K-space sampling and extrapolation," *Magn Reson Med*, vol. 34, no. 5, pp. 686–693, 1995.

[95] S. Posse, S. R. Dager, T. L. Richards, C. Yuan, R. Ogg, A. A. Artru, H.-W. Müller-Gärtner, and C. Hayes, "In vivo measurement of regional brain metabolic response to hyperventilation using magnetic resonance: proton echo planar spectroscopic imaging (pepsi)," *Magnetic resonance in medicine*, vol. 37, no. 6, pp. 858–865, 1997.

[96] S. Posse, G. Tedeschi, R. Risinger, R. Ogg, and D. L. Bihan, "High speed 1h spectroscopic imaging in human brain by echo planar spatial-spectral encoding," *Magnetic resonance in medicine*, vol. 33, no. 1, pp. 34–40, 1995.

[97] M. C. Preul, Z. Caramanos, D. L. Collins, J.-G. Villemure, R. Leblanc, A. Olivier, R. Pokrupa, and D. L. Arnold, "Accurate, noninvasive diagnosis of human brain tumors by using proton magnetic resonance spectroscopy," *Nature medicine*, vol. 2, no. 3, pp. 323–325, 1996.

[98] W. Rock, Y.-L. Li, P. Pagano, and C. M. Cheatum, "2d ir spectroscopy using four-wave mixing, pulse shaping, and ir upconversion: a quantitative comparison," *The Journal of Physical Chemistry A*, vol. 117, no. 29, pp. 6073–6083, 2013.

[99] J. N. Sanders, S. K. Saikin, S. Mostame, X. Andrade, J. R. Widom, A. H. Marcus, and A. Aspuru-Guzik, "Compressed sensing for multidimensional spectroscopy experiments," *The journal of physical chemistry letters*, vol. 3, no. 18, pp. 2697–2702, 2012.

[100] S. Sarkar, K. Heberlein, and X. Hu, "Truncation artifact reduction in spectroscopic imaging using a dual-density spiral k-space trajectory." *Magn Reson Imaging*, vol. 20, no. 10, pp. 743–57, 2002.

[101] S. Sarkar, K. Heberlein, G. J. Metzger, X. Zhang, and X. Hu, "Applications of high-resolution echoplanar spectroscopic imaging for structural imaging," *JMRI*, vol. 10, no. 1, pp. 1–7, 1999.

[102] J. Scheidler, H. Hricak, D. B. Vigneron, K. K. Yu, D. L. Sokolov, L. R. Huang, C. J. Zaloudek, S. J. Nelson, P. R. Carroll, and J. Kurhanewicz, "Prostate cancer: localization with three-dimensional proton mr spectroscopic imaging-clinicopathologic study," *Radiology*, vol. 213, no. 2, pp. 473–480, 1999.

[103] R. Sharma, P. A. Narayana, and J. S. Wolinsky, "Grey matter abnormalities in multiple sclerosis: proton magnetic resonance spectroscopic imaging," *Multiple Sclerosis Journal*, vol. 7, no. 4, pp. 221–226, 2001.

[104] A. Stadlbauer, S. Gruber, C. Nimsky, R. Fahlbusch, T. Hammen, R. Buslei, B. Tomandl, E. Moser, and O. Ganslandt, "Preoperative grading of gliomas by using metabolite quantification with high-spatial-resolution proton mr spectroscopic imaging," *Radiology*, vol. 238, no. 3, pp. 958–969, 2006.

[105] A. Stadlbauer, E. Moser, S. Gruber, R. Buslei, C. Nimsky, R. Fahlbusch, and O. Ganslandt, "Improved delineation of brain tumors: an automated method for segmentation based on pathologic changes of 1 h-mrsi metabolites in gliomas," *Neuroimage*, vol. 23, no. 2, pp. 454–461, 2004.

[106] P. Stoica and R. L. Moses, *Introduction to spectral analysis*. New Jersey, USA: Prentice hall Upper Saddle River, 1997, vol. 1.

[107] Y. Wang and S. J. Li, "Differentiation of metabolic concentrations between gray matter and white matter of human brain by in vivo ^{1}H magnetic resonance spectroscopy," *Magn Reson Med*, vol. 39, no. 1, pp. 28–33, 1998.

[108] J. C. Ye, J. M. Kim, K. H. Jin, and K. Lee, "Compressive sampling using annihilating filter-based low-rank interpolation," *IEEE Transactions on Information Theory*, 2016.

[109] L. Ying and J. Sheng, "Joint image reconstruction and sensitivity estimation in SENSE (JSENSE)," *Magn Reson Med*, vol. 57, no. 6, pp. 1196–1202, 2007.

[110] H. Yu, A. Shimakawa, C. A. McKenzie, E. Brodsky, J. H. Brittain, and S. B. Reeder, "Multiecho water-fat separation and simultaneous R2* estimation with multifrequency fat spectrum modeling," *Magn Reson Med*, vol. 60, no. 5, pp. 1122–1134, 2008.

[111] B. Zhao, J. P. Haldar, C. Brinegar, and Z.-P. Liang, "Low rank matrix recovery for real-time cardiac MRI," in *IEEE International Symposium on Biomedical Imaging: From Nano to Macro, 2010*, 2010, pp. 996–999.